Quantitative mass imaging of single biological macromolecules

Gavin Young,[1,†] Nikolas Hundt,[1,†] Daniel Cole,[1] Adam Fineberg,[1] Joanna Andrecka,[1] Andrew Tyler,[1] Anna Olerinyova,[1] Ayla Ansari,[1] Erik G. Marklund,[2] Miranda P. Collier,[1] Shane A. Chandler,[1] Olga Tkachenko,[1] Joel Allen,[3,§] Max Crispin,[3,§] Neil Billington,[4] Yasuharu Takagi,[4] James R. Sellers,[4] Cédric Eichmann,[5] Philipp Selenko,[5] Lukas Frey,[6] Roland Riek,[6,7] Martin R. Galpin,[1] Weston B. Struwe,[1] Justin L.P. Benesch,[1,*] and Philipp Kukura.[1,*]

Affiliations:

[1]Department of Chemistry, Physical and Theoretical Chemistry Laboratory, South Parks Road, Oxford OX1 3QZ, UK

[2]Department of Chemistry BMC, Uppsala University, Box 576, 75123, Uppsala, Sweden

[3]Oxford Glycobiology Institute, Department of Biochemistry, OX1 3QU, UK

[4]Cell Biology and Physiology Center, National Heart, Lung and Blood Institute, Bethesda, MD 20892, USA

[5]In-Cell NMR Laboratory, Department of NMR-supported Structural Biology, Leibniz Institute of Molecular Pharmacology (FMP Berlin), Robert-Rössle Strasse 10, 13125 Berlin, Germany

[6]Laboratory of Physical Chemistry, Department of Chemistry and Applied Biosciences, ETH Zürich, 8093 Zürich, Switzerland

[7]Department of Immunology and Microbiology, The Scripps Research Institute, 10550 North Torrey Pines Road, La Jolla, California 92037, USA

[§]Present address: Centre for Biological Sciences & Institute for Life Sciences, University of Southampton, Southampton SO17 1BJ, UK

*Correspondence to: justin.benesch@chem.ox.ac.uk; philipp.kukura@chem.ox.ac.uk

[†]These authors contributed equally to this work

Abstract: The cellular processes underpinning life are orchestrated by proteins and their interactions. The associated structural and dynamic heterogeneity, despite being key to function, poses a fundamental challenge to existing analytical and structural methodologies. We use interferometric scattering microscopy to quantify the mass of single biomolecules in solution with 2% sequence mass accuracy, up to 19-kDa resolution, and 1-kDa precision. We resolve oligomeric distributions at high dynamic range, detect small-molecule binding, and mass-image proteins with associated lipids and sugars. These capabilities enable us to characterize the molecular dynamics of processes as diverse as glycoprotein cross-linking, amyloidogenic protein aggregation, and actin polymerization. Interferometric scattering mass spectrometry provides spatio-temporally resolved measurement of a broad range of biomolecular interactions, one molecule at a time.

One Sentence Summary: Light-scattering-based imaging of individual biomolecules allows the spatiotemporal characterization of their interactions and assembly

Biomolecular interactions and assembly are central to a wide range of physiological and pathological processes spanning length scales from small complexes (*1*) to the mesoscale (*2, 3*). Despite considerable developments in techniques capable of providing high-resolution structural information (*4*), they are typically static and involve averaging over many molecules in the sample, and therefore often do not fully capture the diversity of structures and interactions made. Solution-based ensemble methods enable dynamic studies but lack the resolution of separation required to distinguish different species (*5-7*). Single molecule methods offer a means to circumvent heterogeneity in both structure and dynamics, and significant progress has been made in terms of characterizing interactions (*8*) and mechanisms (*9, 10*). There exists no single-molecule approach, however, capable of quantifying and following the diversity of interactions made by biomolecules with sufficient spatiotemporal accuracy and resolution.

Given sufficient sensitivity, light scattering is an ideal means for detecting and characterizing molecules in low-scattering *in vitro* conditions because of its universal applicability. In an interferometric detection scheme (Fig. 1A), the scattering signal scales with the polarizability, which is a function of the refractive index and proportional to the particle volume (*11*). Combining the approximation that single amino acids effectively behave like individual nano-objects with the observation that the specific volumes of amino acids and refractive indices of proteins vary by only ~1% (Fig. S1; Table S1) suggests that the number of amino acids in a polypeptide, and thus its mass, is proportional to its scattering signal. This close relationship between mass and interferometric contrast, which has been predicted (*12, 13*) and observed (*14, 15*) to hold coarsely even at the single molecule level, could thus in principle be used to achieve high mass accuracy.

Building on recent advances in the experimental approach (Fig. S2) that improved imaging contrasts for interferometric scattering microscopy (*15, 16*), we could obtain high quality images of single proteins as they diffuse from solution to bind non-specifically near the interface consisting of a microscope coverslip and the solution (Fig. 1B, Movie S1). Reaching signal-to-noise ratios >10, even for small proteins such as bovine serum albumin (BSA), combined with an optimized data analysis approach (*16*), allowed us to extract the scattering contrast for each molecular binding event with high precision (Fig. 1C, Fig. S3). These led to clear signatures of different oligomeric states, shown here for BSA with relative abundances of 88.63%, 9.94%, 1.18% and 0.25% of the detected particles (Fig. 1D). For non-specific binding to an unfunctionalized microscope coverslip as used here, surface attachment was effectively irreversible (12209 binding vs 372 unbinding events). As a result, we could determine (bulk) binding rate constants, which generally exhibited only small variations with oligomeric state that could be accomodated to obtain minor corrections to the recorded mass spectra and yield the solution distribution (Fig. S4). These results, including the detection and quantification of rare complexes such as BSA tetramers, demonstrate the ability of interferometric scattering mass spectrometry (iSCAMS) to characterize solution distributions of oligomeric species and molecular complexes at high dynamic range.

The regular spacing in the contrast histogram of BSA tentatively confirms the expected linear scaling between mass and interferometric contrast. Repeating these measurements for eight different proteins, spanning 53 – 803 kDa, revealed a linear relationship (Fig. 2A, Fig. S5A). The deviation between measured and sequence mass was <5 kDa, resulting in an average error of 1.9%, and no detectable correlation with refractivity in relation to the overall shape of the molecule (Fig. S6A). Even for large structural differences, such as those between the

extended and folded conformation of smooth-muscle myosin (530.6 kDa, Fig. 2A and Figs. S5B and S7), we did not find measurable differences in the molecular mass beyond the mass increase expected for addition of glutaraldehyde molecules (Extended: 528.4 ± 16.2 kDa, folded: 579.4 ± 14.8 kDa, Fig. S5B) used to crosslink myosin into the folded conformation. The resolution, as defined by the full-width at half-maximum (FWHM) of the measured contrast reached 19 kDa for streptavidin. In all cases, the resolution was limited by photon shot noise and influenced by molecular mass, increasing from 19 kDa for streptavidin to 102 kDa for thyroglobulin (Fig. S6B,C). The sub-0.5% deviation from sequence mass for species of >100 kDa compares well to native mass spectrometry (*17*), and demonstrates the intrinsic utility of iSCAMS for the accurate mass measurement of biomolecules with oligomeric resolution.

Moving beyond species composed solely of amino acids, lipid nanodiscs represent an ideal system for testing the broad applicability of iSCAMS due to their flexibility in terms of polypeptide and lipid content (*18*). For nanodiscs composed of the MSP1D1 belt protein and DMPC lipids, we obtained a mass of 141.0 ± 1.6 kDa, in good agreement with the range of masses reported by other methods, spanning 124 – 158 kDa (Fig. 2B and Fig. S5D). Replacing MSP1D1 with the smaller MSP1ΔH5 reduces the nanodisc diameter and the lipid content by ~20%, after accounting for the thickness of the protein belt (*19*). Given the masses of MSP1D1 and MSP1ΔH5 (47 and 42 kDa, respectively), we predicted a mass for the MSP1ΔH5 nanodisc of 113.6 kDa, in excellent agreement with our measurement (114.1 ± 1.9 kDa). Notably, mass shifts associated with changes in lipid composition, such as those introduced by partially unsaturated lipids and cholesterol, matched those predicted from the assembly ratios (Fig. 2B, Tables S2-S6).

To see whether our approach also applies to solvent-exposed moieties that experience a different dielectric environment to those buried within a protein, we selected the HIV envelope glycoprotein complex (Env), which is a trimer of gp41-gp120 heterodimers. Env is extensively N-glycosylated, with the carbohydrates contributing to almost half of its mass (*20*). For an Env trimer mimic expressed in the presence of kifunensine, a mannosidase inhibitor that leads predominantly to unprocessed $Man_9GlcNAc_2$ glycans (Fig. S8), we recorded a mass of 350.0 ± 5.7 kDa. Making the crude approximation that glycans and amino-acids have similar polarizabilities, this corresponds to a glycan occupancy of 74 ± 3 out of 84 possible sites (Fig. 2C and Fig. S5E), consistent with recent observations of high occupancy for gp120 expressed with kifunensine (*21*). For Env expressed without kifunensine we recorded a lower mass of 315.3 ± 10.5 kDa. The mass difference can only in part be attributed to the lower average mass of the processed glycans (Fig. S8) and yields a total N-glycan occupancy of 61 ± 6. While the exact values for occupancy are beholden to our calibration (Fig. 2A), the presence of unoccupied sites is consistent with their observation in proteomics data (*22*).

The high precision of 1.8 ± 0.5% with respect to the protein mass (Fig. 2A), indicates the potential for direct detection of small-molecule binding. To probe the current limits of iSCAMS in terms of precision, we therefore examined the biotin-streptavidin system (Fig. 2D, Fig. S5C), and measured masses for streptavidin in the absence (55.7 ± 1.1 kDa) and presence (57.4 ± 0.9 kDa) of biotin. This corresponds to a difference of 1.7 ± 1.4 kDa, in good agreement with the expected 0.98 kDa for complete occupancy of the four binding sites. Upon addition of two different biotinylated peptides (3705.9 Da and 4767.4 Da), we obtained increases of 16.1 ± 2.8 kDa and 22.0 ± 2.2 kDa (compared to 14.8 kDa and 19.1 kDa expected) (Fig. 2D, Fig. S5C).

These data show that iSCAMS can detect the association of kDa-sized ligands, demonstrating its suitability for highly sensitive ligand-binding studies in solution.

After having established the capabilities of iSCMAS, we sought to test it on more complex systems that are difficult to assess quantitatively with existing techniques as a consequence of heterogeneity and multi-step assembly mechanisms (Fig. 3). In addition, we aimed to monitor nucleation and polymerization dynamics of mesoscopic structures down to the single molecule level, which are challenging because of the simultaneous requirement for high dynamic range, imaging speed and direct correlation between the observed signals and the associated molecular events. The biotin-streptavidin system exhibits nearly covalent binding, raising the question whether iSCAMS is capable of not only determining mass distributions but also of quantifying weaker equilibria, as often encountered for protein-protein interactions.

We therefore investigated the interaction of Env with the anti-viral lectin BanLec, which neutralises HIV by binding to surface N-glycans(*23*, *24*) via an unknown mechanism. We could monitor the interactions and short-lived complexes prior to aggregation, with the addition of BanLec to Env resulting in a reduction of single Env units coupled to the appearance of dimers and higher-order assemblies (Fig. 3A). The experimental oligomeric evolution coupled with a simple model (Fig. 3B) enabled us to extract the underlying association constants (K_{BanLec} = 0.12 nM^{-1}, K_{Env} = 8 nM^{-1}, K'_{BanLec} = 0.4 nM^{-1}), in good agreement with recent bulk studies (K_{BanLec} = 0.19 nM^{-1}), which also observed signatures of and estimated the energetics of a secondary binding event (K_2 = 2.85 nM^{-1}) (*25*). Our ability to follow and model the evolution of different oligomeric species allowed us to directly extract the interaction mechanism and the energetics underlying the lectin-glycoprotein interaction, despite the heterogeneity of this multi-component system. As a result, we can show that binding of Env to BanLec that is already bound to Env is

much stronger than to free BanLec, a key characteristic of cooperative behavior. Moreover, the mass resolution of our approach enabled us to quantify the number of BanLecs bound per dimer (1-2), trimer (2-3) and tetramer (3-4) of Env, demonstrating bivalent binding. These results are directly relevant to the characterization and optimization of anti-retrovirals, given that multivalency and aggregation have been proposed to be directly linked to neutralization potency(*25*). We anticipate similar quantitative insights to be achievable for other therapeutic target proteins and protein-protein interactions in general.

An advantage of our imaging-based approach stems from its ability to time-resolve mass changes in a position- and local concentration-sensitive manner. This enables us to examine surface-catalyzed nucleation events that may eventually lead to amyloid formation (*26*). Previous studies using fluorescence labeling found aggregates of ~0.6 μm diameter within a minute of addition of the amyloidogenic protein α-synuclein at 10 μM to an appropriately charged bilayer (*27*). Upon adding α-synuclein to a planar, negatively charged DOPC/DOPS (3:1) membrane at physiological pH, we observed the appearance and growth of nanoscopic objects within seconds, even at low μM concentrations (Fig. 4A, Movie S2). While we were unable to determine the sizes of initial nucleating species or individual assembly steps, given the low molecular mass of α-synuclein (14 kDa), we could nevertheless monitor the nanoscale formation of associated structures in the range of hundreds of kDa and determine the kinetics (Fig. 4B). Growth of these clusters was uniform across the field of view, with the initial rates following expectations for a first-order process (Fig. 4B and Fig. S9A), pointing towards a simple growth mechanism. We did not detect such structures on neutral, DOPC-only bilayers, and found evidence for thioflavin-T positive aggregates after overnight incubation (Fig. S9B), suggesting that our assay probes early stages of amyloid assembly.

At the extremes of our current sensitivity, iSCAMS enables mass-imaging of mesoscopic self-assembly, molecule-by-molecule. In an actin polymerization assay, subtraction of the constant background revealed growth of surface-immobilized filaments. In contrast to α-synuclein, where the growth of interest took place within a diffraction-limited spot, here we could quantify length changes of filaments larger than the diffraction limit upon the attachment and detachment of actin subunits (Fig. 4C, Fig. S10C, Movie S3). We observed distinct, step-wise changes in the filament length (Fig. 4D, Supplementary Fig. S10D-F and Movie S4), the most frequent forward and backward step sizes in the traces being 3.0 ± 0.8 nm and 2.7 ± 0.7 nm, respectively, remarkably close to the expected length increase of 2.7 nm upon binding of a single actin subunit to a filament (Fig. 4E). Detection of larger step sizes represents the addition of multiple actin subunits within our detection time window. The contrast changes associated with the different step sizes corresponded to mass changes of one, two, or three actin monomers binding to and unbinding from the tip of the growing filaments during acquisition (Fig. S10G,H). Even though we cannot yet distinguish between models invoking monomer (*28*) or oligomer (*29*) addition to a growing filament at our current level of spatio-temporal resolution, these results demonstrate the capability of iSCAMS for quantitatively imaging mesoscopic dynamics, and how they are influenced by associated proteins at the single molecule level.

We anticipate that combining iSCAMS with established surface modifications (*30*) will dramatically expand its capabilities. Passivation decreases surface binding probabilities and thereby should provide access to much higher analyte concentrations (>μM), while surface activation will reduce measurement times at low concentrations (<nM). Specific functionalization and immobilization of individual subunits or binding partners could also allow for the determination of on and off rates in addition to equilibrium constants, and enable targeted

detection in the presence of other analytes. Although studies within complex three-dimensional environments like the cell may prove to be beyond reach, these advances will make iSCAMS a powerful approach for dynamic *in vitro* studies of biomolecular interactions, assembly and structure at the single molecule level.

References and Notes:

1. S. E. Ahnert, J. A. Marsh, H. Hernandez, C. V. Robinson, S. A. Teichmann, Principles of assembly reveal a periodic table of protein complexes. *Science*. **350**, aaa2245 (2015).

2. K. Rottner, J. Faix, S. Bogdan, S. Linder, E. Kerkhoff, Actin assembly mechanisms at a glance. *J. Cell Sci.* **130**, 3427–3435 (2017).

3. M. Hemmat, B. T. Castle, D. J. Odde, Microtubule dynamics: moving toward a multi-scale approach. *Curr. Opin. Cell Biol.* **50**, 8–13 (2018).

4. H.-W. Wang, J.-W. Wang, How cryo-electron microscopy and X-ray crystallography complement each other. *Protein Sci.* **26**, 32–39 (2017).

5. D. M. Kanno, M. Levitus, Protein Oligomerization Equilibria and Kinetics Investigated by Fluorescence Correlation Spectroscopy: A Mathematical Treatment. *J. Phys. Chem. B.* **118**, 12404–12415 (2014).

6. M. Chakraborty *et al.*, Protein Oligomerization Monitored by Fluorescence Fluctuation Spectroscopy: Self-Assembly of Rubisco Activase. *Biophys. J.* **103**, 949–958 (2012).

7. S. I. A. Cohen, M. Vendruscolo, C. M. Dobson, T. P. J. Knowles, From Macroscopic Measurements to Microscopic Mechanisms of Protein Aggregation. *J. Mol. Biol.* **421**, 160–171 (2012).

8. A. Jain *et al.*, Probing cellular protein complexes using single-molecule pull-down. *Nature*. **473**, 484–488 (2011).

9. B. Schuler, W. A. Eaton, Protein folding studied by single-molecule FRET. *Curr. Opin. Struct. Biol.* **18**, 16–26 (2008).

10. W. J. Greenleaf, M. T. Woodside, S. M. Block, High-resolution, single-molecule measurements of biomolecular motion. *Annu. Rev. Biophys. Biochem. Struct.* **36**, 171–190 (2007).

11. C. F. Bohren, D. R. Huffman, *Absorption and scattering of light by small particles* (Wiley Interscience, New York, 1983).

12. P. Kukura *et al.*, High-speed nanoscopic tracking of the position and orientation of a single virus. *Nat. Meth.* **6**, 923–927 (2009).

13. J. Ortega Arroyo *et al.*, Label-free, all-optical detection, imaging, and tracking of a single protein. *Nano Lett.* **14**, 2065–2070 (2014).

14. M. Piliarik, V. Sandoghdar, Direct optical sensing of single unlabelled proteins and super-resolution imaging of their binding sites. *Nat. Commun.* **5**, 4495 (2014).

15. M. Liebel, J. T. Hugall, N. F. van Hulst, Ultrasensitive Label-Free Nanosensing and High-Speed Tracking of Single Proteins. *Nano Lett.* **17**, 1277–1281 (2017).

16. D. Cole, G. Young, A. Weigel, A. Sebesta, P. Kukura, Label-Free Single-Molecule Imaging with Numerical-Aperture Shaped Interferometric Scattering Microscopy. *ACS Photonics*. **4**, 211–216 (2017).

17. M. van de Waterbeemd *et al.*, High-fidelity mass analysis unveils heterogeneity in intact ribosomal particles. *Nat. Meth.* **14**, 283–286 (2017).

18. I. G. Denisov, S. G. Sligar, Nanodiscs in Membrane Biochemistry and Biophysics. *Chem. Rev.* **117**, 4669–4713 (2017).

19. S. Bibow *et al.*, Solution structure of discoidal high-density lipoprotein particles with a shortened apolipoprotein A-I. *Nat. Struct. Mol. Biol.* **24**, 187–193 (2017).

20. L. A. LASKY *et al.*, Neutralization of the Aids Retrovirus by Antibodies to a Recombinant Envelope Glycoprotein. *Science*. **233**, 209–212 (1986).

21. W. B. Struwe, A. Stuckmann, A.-J. Behrens, K. Pagel, M. Crispin, Global N-Glycan Site Occupancy of HIV-1 gp120 by Metabolic Engineering and High-Resolution Intact Mass Spectrometry. *ACS Chem. Biol.* **12**, 357–361 (2017).

22. L. Cao *et al.*, Global site-specific N-glycosylation analysis of HIV envelope glycoprotein. *Nat. Commun.* **8**, 14954 (2017).

23. M. D. Swanson, H. C. Winter, I. J. Goldstein, D. M. Markovitz, A lectin isolated from bananas is a potent inhibitor of HIV replication. *J. Biol. Chem.* **285**, 8646–8655 (2010).

24. J. T. S. Hopper *et al.*, The Tetrameric Plant Lectin BanLec Neutralizes HIV through Bidentate Binding to Specific Viral Glycans. *Structure*. **25**, 773–782 (2017).

25. S. Lusvarghi *et al.*, Binding Site Geometry and Subdomain Valency Control Effects of Neutralizing Lectins on HIV-1 Viral Particles. *ACS Infect. Dis.* **2**, 882–891 (2016).

26. C. Galvagnion *et al.*, Lipid vesicles trigger alpha-synuclein aggregation by stimulating primary nucleation. *Nat. Chem. Biol.* **11**, 229–234 (2015).

27. A. Iyer, N. Schilderink, M. M. A. E. Claessens, V. Subramaniam, Membrane-Bound Alpha Synuclein Clusters Induce Impaired Lipid Diffusion and Increased Lipid Packing. *Biophys. J.* **111**, 2440–2449 (2016).

28. M. Kasai, F. Oosawa, S. Asakura, Cooperative Nature of G-F Transformation of Actin. *Biochim. Biophys. Acta*. **57**, 22–31 (1962).

29. H. P. Erickson, Co-Operativity in Protein-Protein Association - the Structure and Stability of the Actin Filament. *J. Mol. Biol.* **206**, 465–474 (1989).

30. B. Hua *et al.*, An improved surface passivation method for single-molecule studies. *Nat. Meth.* **11**, 1233–1236 (2014).

31. T. L. McMeekin, M. L. Groves, M. Wilensky, Refractive Indices of Proteins in Relation to Amino Acid Composition and Specific Volume. *Biochem. Biophys. Res. Commun.* **7**, 151–156 (1962).

32. Y. Harpaz, M. Gerstein, C. Chothia, Volume Changes on Protein-Folding. *Structure*. **2**, 641–649 (1994).

33. A. Yildiz *et al.*, Myosin V walks hand-over-hand: Single fluorophore imaging with 1.5-nm localization. *Science*. **300**, 2061–2065 (2003).

34. N. Billington, A. Wang, J. Mao, R. S. Adelstein, J. R. Sellers, Characterization of Three Full-length Human Nonmuscle Myosin II Paralogs. *J. Biol. Chem.* **288**, 33398–33410 (2013).

35. J. R. Sellers, M. D. Pato, R. S. Adelstein, Reversible Phosphorylation of Smooth-Muscle Myosin, Heavy-Meromyosin, and Platelet Myosin. *J. Biol. Chem.* **256**, 3137–3142 (1981).

36. L. Yang *et al.*, An adaptive non-local means filter for denoising live-cell images and improving particle detection. *J. Struct. Biol.* **172**, 233–243 (2010).

37. M. S. Woody, J. H. Lewis, M. J. Greenberg, Y. E. Goldman, E. M. Ostap, MEMLET: An Easy-to-Use Tool for Data Fitting and Model Comparison Using Maximum-Likelihood Estimation. *Biophys. J.* **111**, 273–282 (2016).

38. C. Tzitzilonis, C. Eichmann, I. Maslennikov, S. Choe, R. Riek, Detergent/Nanodisc Screening for High-Resolution NMR Studies of an Integral Membrane Protein Containing a Cytoplasmic Domain. *PLoS ONE*. **8**, e54378 (2013).

39. R. W. Sanders *et al.*, A Next-Generation Cleaved, Soluble HIV-1 Env Trimer, BG505 SOSIP.664 gp140, Expresses Multiple Epitopes for Broadly Neutralizing but Not Non-Neutralizing Antibodies. *Plos Pathogens*. **9**, e1003618 (2013).

40. S. Campioni *et al.*, The Presence of an Air-Water Interface Affects Formation and Elongation of alpha-Synuclein Fibrils. *J. Am. Chem. Soc.* **136**, 2866–2875 (2014).

41. S. S. Lehrer, G. Kerwar, Intrinsic Fluorescence of Actin. *Biochemistry*. **11**, 1211–1217 (1972).

42. F. Ruhnow, D. Zwicker, S. Diez, Tracking Single Particles and Elongated Filaments with Nanometer Precision. *Biophys. J.* **100**, 2820–2828 (2011).

43. Chen, J., & Gupta, A. K. Testing and Locating Variance Changepoints with Application to Stock Prices. *J. Am. Stat. Assoc.*, **92**, 739 (1997).

44. K. C. Holmes, D. Popp, W. Gebhard, W. Kabsch, Atomic Model of the Actin Filament. *Nature*. **347**, 44–49 (1990).

45. T. D. Pollard, M. S. Mooseker, Direct Measurement of Actin Polymerization Rate Constants by Electron-Microscopy of Actin-Filaments Nucleated by Isolated Microvillus Cores. *J. Cell Biol.* **88**, 654–659 (1981).

46. T. D. Pollard, Rate Constants for the Reactions of ATP-Actin and ADP-Actin with the Ends of Actin-Filaments. *J. Cell Biol.* **103**, 2747–2754 (1986).

47. E. G. Marklund, M. T. Degiacomi, C. V. Robinson, A. J. Baldwin, Benesch, Justin L. P., Collision Cross Sections for Structural Proteomics. *Structure*. **23**, 791–799 (2015).

48. F. Hagn, M. Etzkorn, T. Raschle, G. Wagner, Optimized Phospholipid Bilayer Nanodiscs Facilitate High-Resolution Structure Determination of Membrane Proteins. *J. Am. Chem. Soc.* **135**, 1919–1925 (2013).

49. M. T. Marty *et al.*, Native Mass Spectrometry Characterization of Intact Nanodisc Lipoprotein Complexes. *Anal. Chem.* **84**, 8957–8960 (2012).

50. I. G. Denisov, Y. V. Grinkova, A. A. Lazarides, S. G. Sligar, Directed self-assembly of monodisperse phospholipid bilayer nanodiscs with controlled size. *J. Am. Chem. Soc.* **126**, 3477–3487 (2004).

Acknowledgments:

JRS thanks Fang Zhang for technical assistance and the NHLBI electron microscopy core facility. GY was supported by a Zvi and Ofra Meitar Magdalen Graduate Scholarship; NH by a DFG research fellowship (HU 2462/1-1). EGM thanks the Swedish Research Council and the European Commission for a Marie Skłodowska Curie International Career Grant (2015-00559). MPC is a Clarendon Scholar supported by the Oxford University Press. SAC is supported by the Biotechnology and Biological Sciences Research Council and Waters Corp by the iCASE studentship BB/L017067/1 to JLPB. OT acknowledges a Lamb and Flag Scholarship from St John's College, University of Oxford and an EPSRC Studentship. JA and MC were supported by the National Institute of Allergy and Infectious Diseases (Center for HIV/AIDS Vaccine Immunology and Immunogen Discovery grant UM1AI100663). JRS was supported by NHLBI Intramural program HL0001786. CE is supported by a SNSF advanced postdoctoral mobility fellowship (P300PA160979). PS is funded by an ERC Consolidator Grant (NeuroInCellNMR, 647474). JLPB thanks the Engineering and Physical Sciences Research Council for EP/J01835X/1. PK was supported by an ERC Starting Investigator Grant (Nanoscope, 337577).

Conceptualization, WBS, JLPB and PK; Methodology GY, NH, DC, JA, EGM, CE, PS, MRG, WBS, JLPB, PK; Software GY, NH; Validation GY, NH, JLPB, PK; Formal analysis, GY, NH, AT, AA, AO, JA, EGM, MRG; Investigation GY, NH, DC, AF, JA, AT, AA, NB, YT, CE; Resources MPC, SAC, OT, JA, MC, NB, YT, JRS, CE, PS, LF, RR, WS; Writing - original draft GY, JLPB, PK; Writing - review and editing GY, NH, AF, AO, EGM, MPC, SAC, OT, MC, JRS, CE, PS, RR, MRG, WBS, JLPB, PK; Visualization GY, NH, JLPB, PK; Supervision PK.

GY, DC and PK have filed a patent on the contrast enhancement methodology and its application to mass measurement of single biomolecules. All other authors declare no competing interests.

All data necessary to support the conclusions are available in the manuscript or supplementary materials and are deposited with the University of Oxford Research Archive (ORA) with 10.5287/bodleian:PmA5Va0a2

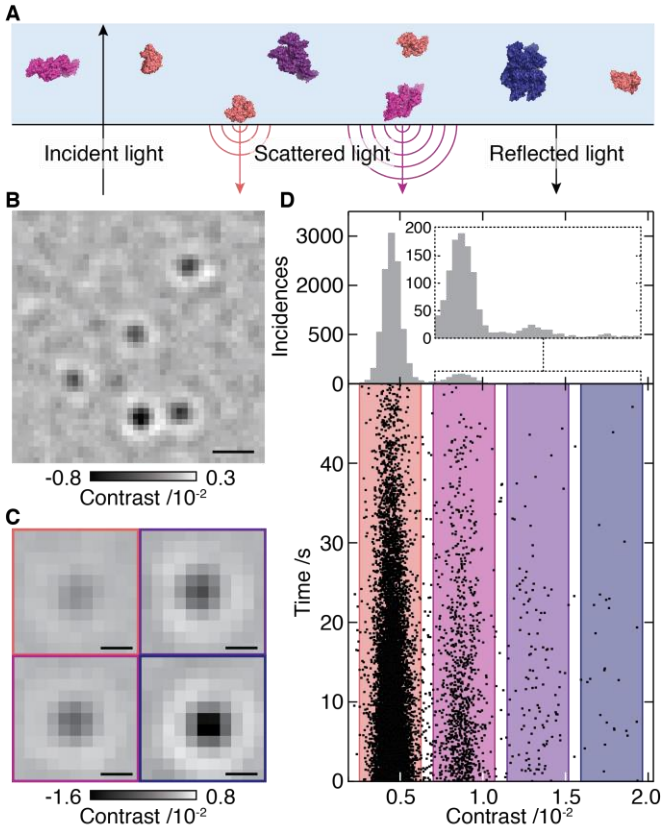

Fig. 1. **Concept of interferometric scattering mass spectrometry (iSCAMS).** (**A**) Schematic of the experimental approach relying on immobilization of individual molecules near a refractive index interface. Oligomeric states are coloured differently for clarity. (**B**) Differential interferometric scattering image of BSA. Scale bar: 0.5 μm. (**C**) Representative images of monomers, dimers, trimers and tetramers of BSA. Scale bar: 200 nm. (**D**) Scatter plot of single molecule binding events and their scattering contrasts for 12 nM BSA from 14 movies (lower). Corresponding histogram (N=12209) and zoom of the region for larger species (upper). The reduction in landing rate results from a drop in BSA concentration with time due to the large surface-to-volume ratio of our sample cell (see Supplementary Information).

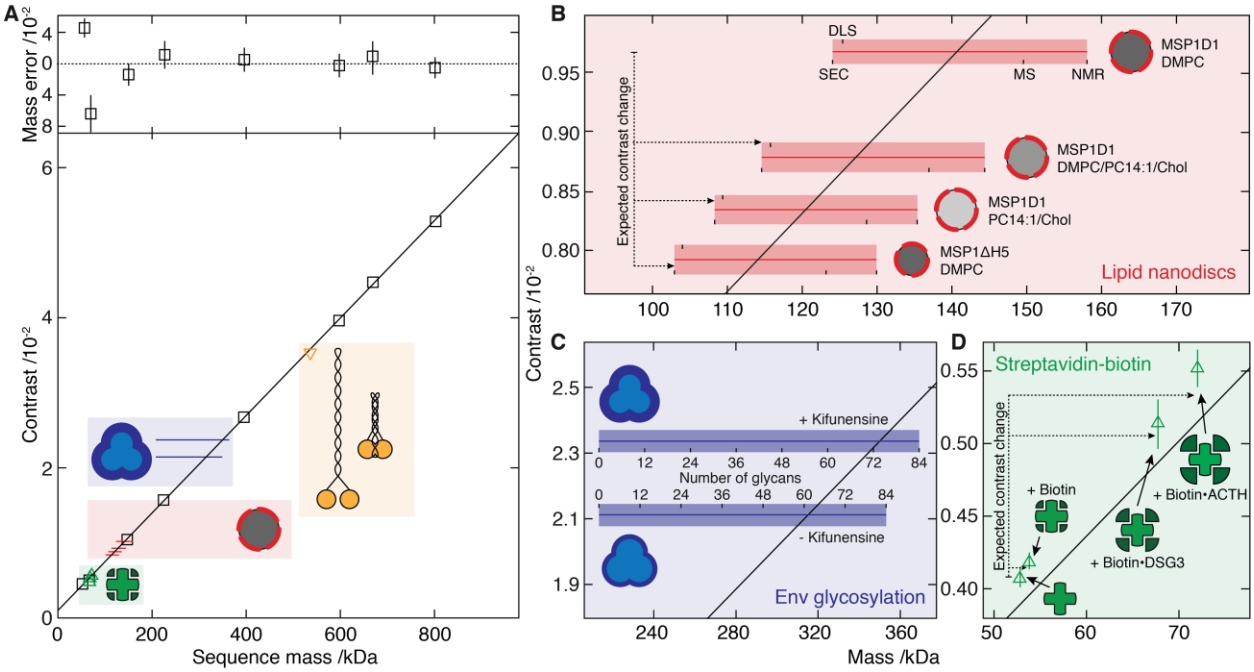

Fig. 2. Characterization of iSCAMS accuracy, precision, and dependence on molecular shape and identity. (**A**) Contrast vs molecular mass including proteins used for mass calibration (black), characterization of shape dependence (yellow), protein-ligand binding (green), lipid nanodisc composition (red) and glycosylation (blue). Mass error (upper panel) is given as a percentage of the sequence mass relative to the given linear fit. (**B**) Nanodisc mass-measurement for different lipid compositions and protein belts. Masses obtained by alternative methodologies for MSP1D1/DMPC are marked and extrapolated to the other compositions. The horizontal bars indicate the expected mass range as a function of characterization technique, with the thin bar indicating the contrast measured, and the thick bar representative of the measurement uncertainty in terms of the standard error of the mean for repeated experiments. For each sample, the upper text denotes the membrane scaffold protein (MSP) used, and the lower the lipids in the nanodisc. (**C**) Recorded differential contrast for Env expressed in the presence or absence of kifunensine, and associated mass ranges expected for different glycosylation levels. (**D**) Mass-sensitive detection of ligand binding using the biotin-streptavidin system according to the sequence mass

of streptavidin and the masses of biotin and two biotinylated peptides relative to the calibration obtained from **A**. Abbreviations used are summarized in Supplementary Table S8.

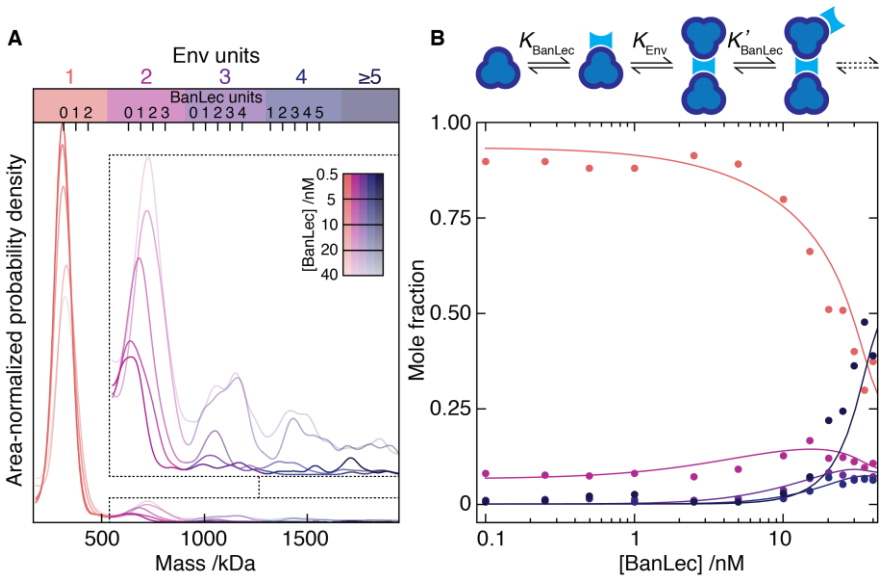

Fig. 3. **Single molecule mass analysis of heterogeneous protein assembly.** (**A**) Mass distributions for Env in the presence of 0.5 – 40 nM BanLec monomer. Inset: zoom alongside expected positions for multiples of bound BanLec tetramers. (**B**) Oligomeric fractions colored according to **A** vs BanLec concentration including predictions (solid) using the given cooperative model.

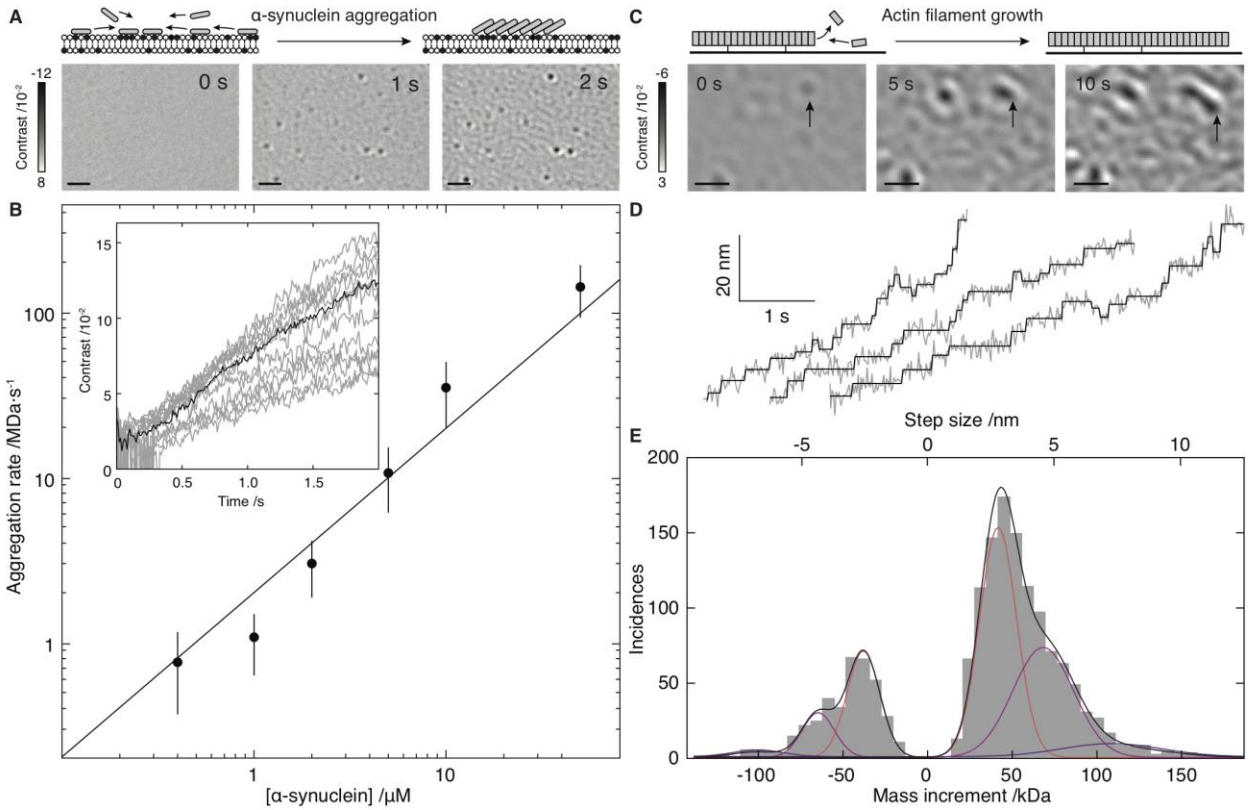

Fig. 4. **Mass-imaging of mesoscopic dynamics.** (**A**) Schematic of and iSCAMS images for α-synuclein (1 μM) aggregation on a negatively charged bilayer membrane. (**B**) Initial growth rate vs. α-synuclein concentration alongside the best fit assuming first order kinetics (solid). Inset: Individual growth trajectories (grey) and average (black) for 21 particles from **A**. (**C**) Schematic and iSCAMS images of actin polymerization. The arrow highlights a growing filament. (**D**) Representative traces of actin filament tip position (grey) and corresponding detected steps (black). (**E**) Step and mass histogram from 1523 steps and 33 filaments including a fit to a Gaussian mixture model (black) and individual contributions (colored). Scale bars: 1 μm. In these experiments, background correction involved removal of the static background prior to acquisition, rather than continuous differential imaging as in Figs. 2 and 3 (see Supplementary Information).

Supplementary Materials:

Materials and Methods

Figures S1-S10

Tables S1-S8

Movies S1-S4

References 31-51

Supplementary Materials for

Quantitative mass imaging of single molecules

Gavin Young, Nikolas Hundt, Daniel Cole, Adam Fineberg, Joanna Andrecka, Andrew Tyler, Anna Olerinyova, Ayla Ansari, Erik G. Marklund, Miranda P. Collier, Shane A. Chandler, Olga Tkachenko, Joel Allen, Max Crispin, Neil Billington, Yasuharu Takagi, James R. Sellers, Cedric Eichmann, Philipp Selenko, Lukas Frey, Roland Riek, Martin R. Galpin, Weston B. Struwe, Justin L. P. Benesch, and Philipp Kukura

correspondence to: philipp.kukura@chem.ox.ac.uk

This PDF file includes:

Materials and Methods
Figs. S1 to S10
Tables S1 to S8
Captions for Movies S1 to S4

Other Supplementary Materials for this manuscript includes the following:

Movies S1 to S4

Materials and Methods

Protein volume and refractive index calculation

All protein sequences from *Escherichia coli*, *Yersinia pestis*, *Haloferax volcanii*, *Methanocadococcus jannaschii*, *Homo sapiens*, and *Arabidopsis thaliana* genomes were downloaded from NCBI (https://www.ncbi.nlm.nih.gov/genome/) in FASTA format. The refractive index of each protein was calculated as

$$n = \sqrt{\frac{\left(\frac{2MR}{VN} + 1\right)}{\left(1 - \frac{R}{V}\right)}}$$

where $M = M_w + \sum_i (M_i - M_w)$ is the molar mass of the protein, determined from the sequence, and where the M_W–terms represent the loss of one water molecule per peptide bond; $R = \sum_i n_i$, is the sum of contributions from individual amino acid residues(*31*); $V = \sum_i V_i$, the specific volume, also determined from the contribution of individual residues (*32*); and *N* is the number of residues. M_i, n_i, and V_i were determined from the residue type (Table S1). Wherever ambiguous FASTA codes were encountered (B, J, X, and Z), parameters (M_i, n_i, and V_i) were set to the arithmetic average for the possible residue types (e.g., the average of D and N for FASTA code B).

Microscope coverslip cleaning procedure

We cleaned borosilicate microscope coverslips (No. 1.5, 24 × 50 mm^2, VWR, and No. 1.5, 24 × 24 mm^2, VWR) by rinsing them sequentially with H_2O, ethanol, H_2O, isopropanol, H_2O, ethanol and H_2O, followed by drying under a clean stream of nitrogen.

Landing assay procedure

Cleaned coverslips were assembled into flow chambers(*33*). Buffers were filtered through a 0.2 μm pore size syringe filter. All samples were diluted from stock solutions without further treatment. Sample proteins were diluted in 20 mM Tris-HCl, 100 mM NaCl, pH 7.4, unless otherwise stated. Typical working concentrations were 5 − 10 nM of the predominant species. After filling the flow chamber with buffer, a clean region of interest in the flow chamber was selected defined as being devoid of large scatterers on the surface, followed by flushing in 10 μl

of the protein solution.

Calibration Proteins

Streptavidin (2105), bovine serum albumin (BSA, 2571), alcohol dehydrogenase (ADH, 8066), β −amylase (βA, 9988), thyroglobulin (2951) and GroEL (3955) were purchased from Sigma-Aldrich. Non-muscle myosin 2B (10042) was purified as described previously(*34*), except for the addition of a halo-tag. The numbers in parentheses indicate the total number of detected particles for each calibrant from 4 − 10 separate experiments.

Myosin crosslinking

Smooth-muscle myosin (SMM) was purified as described previously (*35*) and incubated at 200 nM in ATP-containing buffer (10 mM MOPS, 150 mM NaCl, 1 mM $MgCl_2$, 0.1 mM EGTA, 0.1 mM ATP, pH 7.0) for 30 min, which induced the folded (10S) conformation. Glutaraldehyde was added to a concentration of 0.1% (v/v) and incubated for 1 min. The reaction was stopped by addition of Tris-HCl (pH 8.0) to a final concentration of 100 mM.

Electron Microscopy

Cross-linked myosin was diluted to 20 nM in buffer containing 10 mM MOPS, 150 mM NaCl, 1 mM $MgCl_2$, 0.1 mM EGTA, pH 7.0. Native myosin was diluted to 5 nM in buffer containing 10 mM MOPS, 500 mM NaCl, 1 mM $MgCl_2$, 0.1 mM EGTA, pH 7.0, which induced the extended conformation. 3 μl of sample was applied to a carbon-coated copper grid (pretreated for 45 minutes with ultraviolet light) and stained with 1% uranyl acetate. Micrographs were recorded on a JEOL 1200EX II microscope operating at room temperature. Data were collected on an AMT XR-60 CCD camera.

iSCAMS measurements of smooth-muscle myosin

Native (6S) and cross-linked (10S) myosins were diluted in buffer containing 10 mM MOPS, 500 mM NaCl, 1 mM $MgCl_2$, 0.1 mM EGTA, pH 7.0, to a concentration of 5 nM and kept on ice until use. The landing assay was performed in a flow chamber as described above.

Biotin-streptavidin binding assay

Streptavidin (Cat no. S4762) and D-biotin (Cat no. B4501) were purchased from Sigma Aldrich. Two synthetic N-terminally biotinylated peptides based on the sequences of desmoglein-3 (DSG3, biotin-EWVKFAKPCREGEDNSKRNPIAKITSDYQA) and adrenocorticotropic hormone (ACTH, biotin-

SYSMEHFRWGKPVGKKRRPVKVYPNGAEDESAEAFPLEF) were bought from Cambridge Research Biochemicals. Samples of 5 nM streptavidin and mixes of 5 nM streptavidin with 500 nM of either biotin, biotin-DSG3 peptide or biotin-ACTH peptide were prepared at the start of the day and kept on ice until use. The total number of detected particles in 4 − 9 experiments were 2105, 2167, 3131 and 936 for streptavidin, biotin-streptavidin, biotin-DSG3-streptavidin and biotin-ACTH-streptavidin, respectively.

Experimental Setup

The experimental setup is depicted schematically in Fig. S2, and is identical to that described in Fig. 4 of Cole et al.(*16*), except for the apparatus being mounted onto a 400x600x50 mm^3 aluminium plate and enclosed to minimize the influence of external perturbations. Briefly, the collimated output of a 445 nm laser diode (Lasertack) is passed through an orthogonal pair of acousto-optic deflectors (AODs; AA Opto Electronic, DT SXY-400). A 4f telecentric lens system (Telecentric lens 1, and Telecentric lens 2) images the deflection of the beam by the AODs into the back focal plane of the microscope objective (Olympus, 1.42 NA, 60×) after passing through a polarizing beam splitter (PBS) and a quarter-wave-plate (QWP). This results in a weakly focused beam (spot size 1.5 μm) being scanned across the sample to generate the field of view. The objective collects the light reflected at the glass-water interface together with that back-scattered by the sample, which is separated from the incident light by the combination of the PBS and QWP. A second 4f telecentric system (Lens 1 and Lens 2) reimages the back focal plane of the objective, where a partially reflective mirror consisting of a 3.5 mm diameter thin layer of silver deposited onto a window selectively attenuates the reflected light by more than two orders of magnitude with respect to light from point scatterers at the surface (*16*). A final lens (Lens 3) images the sample onto a CMOS camera (Point Grey GS3-U3-23S6M-C) with 250× magnification, giving a pixel size of 23.4 nm/pixel. The focus position is stabilized with an active feedback loop using a total internally-reflected beam (not shown).

Data acquisition parameters

The camera was run close to the highest frame rate achievable for the given field of view, typically 1 kHz. Unless otherwise stated, images were pixel-binned 3x3 and time-averaged 10-fold prior to saving, giving a final pixel size of 70.2 nm and effective frame rate of 100 Hz. The power density, frame rate, exposure time and effective exposure time after averaging were: Figs. 1B-D, 2D, S3, S4A and E, S5C, S6B: 860 kW/cm^2, 1000 Hz, 0.95 ms, 47.5 ms; Figs. 2A, 3, S4F,

S5A and E, S6A and C: 420 kW/cm^2, 662 Hz, 1.5 ms, 300 ms; Fig. S5B: 500 kW/cm^2, 662 Hz, 1.5 ms, 300 ms; Figs. 2B and C, S5D and E: 280 kW/cm^2, 662 Hz, 1.5 ms, 300 ms; Figs. 4A and B, S9A: 45 kW/cm^2, 100 Hz, 9.9 ms; Figs. 4C-E, S10: 88 kW/cm^2, 468 Hz, 2.1 ms, 16.8 ms.

Image processing: background removal

Unless otherwise stated, analysis was performed using custom software written in LabVIEW. To remove the static scattering background from the glass surface (Fig. S3A), ratiometric images, R, were calculated as $R = N_{m+1}/N_m - 1$, where N_m are consecutive normalized averages of several images, revealing only those features that change between the two frame batches (Fig. S3B). Each frame batch is normalized by the mean pixel value before generating the ratiometric image to avoid effects caused by slow laser intensity fluctuations. This processing is stepped through the raw movie frame-by-frame, generating a ratiometric frame stack in which a binding event appears as a (dark) point spread function (PSF), the contrast of which increases and then decreases as the midpoint of the two frame batches approaches and then moves past the time at which the protein binds (Fig. S3C,D). Unbinding events, meanwhile, appear as bright spots and are insignificant in number compared to binding events for landing assays on bare glass. For example, for the data shown in Fig. 1, we observed 12209 binding vs 372 unbinding events.

Image processing: particle detection and quantification

Particles were identified in the ratiometric images by an automated spot detection routine. As a first step, the convolution of the ratiometric image with the experimentally measured PSF was calculated to assist with particle detection. From the resulting image, a particle probability (PP) image was calculated as described previously(*36*), and pixels with PP > 0.3 that also corresponded to a local maximum in the convolved image were taken as candidate particles.

About each candidate pixel, an 11×11 pixel^2 (772×772 nm^2) region of interest was extracted and fit to a model PSF to extract the contrast. In place of the more conventional 2D Gaussian function, we used a difference of two concentric 2D Gaussians to model the effect of the circular partial reflector in the Fourier plane on the PSF(*16*). The width and amplitude of the second Gaussian (arising from the presence of the partial reflector) were dictated by the relative sizes of the partial reflector and objective back aperture, and the reflectance of the mask, thus avoiding additional parameters in the fit:

$$f(x,y) = A\left(e^{-\left[\frac{(x-x_0)^2}{2\sigma_x^2}+\frac{(y-y_0)^2}{2\sigma_y^2}\right]} - \frac{(1-T)}{s} e^{-\left[\frac{(x-x_0)^2}{2(s\sigma_x)^2}+\frac{(y-y_0)^2}{2(s\sigma_y)^2}\right]} \right) + b$$

where $s = 8.52/3.5$, is the ratio between the diameter of the objective back aperture and the diameter of the partial reflector, and T is the transmission of the mask. The contrast reported is therefore $A\left(1 - \frac{(1-T)}{s}\right)$, corresponding to the peak value of this function as it appears in an image. If the fitted function was too eccentric it was rejected as not arising from a single molecule binding event. This was determined by taking the ratio of the smaller to the larger of the two fitted standard deviations (σ_x and σ_y), and rejecting the fit if this ratio was below 0.7.

As described above, the sliding ratiometric analysis results in a single molecule binding event appearing in several consecutive frames, with increasing and then decreasing contrast. To avoid over-counting particles, and to extract the most accurate measure of the particle contrast, the fits were grouped into those arising from a single particle based on their spatial and temporal location in the image stack. Points lying within 1 pixel of each other and arising from frames within a window size of twice the temporal frame averaging were classified as one particle. The contrast of a given particle as a function of time in the image stack then exhibits a linear growth up to a maximum, followed by a linear decrease. For each particle, this profile was fit to a pair of straight lines with gradients of equal magnitude but opposite sign, and the peak contrast taken to be the best estimate of the true particle contrast (Fig. S3D).

To extract accurate values for the mean contrast (Fig. 2), the resulting contrast distribution was fit to one or the sum of two Gaussian peaks (a Gaussian function when a single peak was well-isolated from other detected species, or the sum of two Gaussians where two peaks were not fully separated). Fitting was performed using the maximum-likelihood procedure as implemented in MEMLET(*37*). To optimize the fit by maximum-likelihood, it was necessary to reject outlying data points from the distribution (e.g. from the presence of some smaller species in solution, or larger aggregates). For unimodal distributions, for example, outliers were defined as those points either with a contrast less than the lower quartile minus 1.5 times the interquartile range, or greater than the upper quartile plus 1.5 times the interquartile range.

The dependence on sequence mass of the average value of the contrast determined in this way for each of the 8 proteins listed above was fit to a straight line in order to calibrate the system. We used the difference between the line of best fit and the measured data to assess the accuracy

of the technique, resulting in the average deviation of 1.9% from the sequence mass reported in the main text.

Surface vs solution distributions and corrections

In landing assays, we detect individual molecules binding to the cover glass surface, rather than directly in solution. As a result, variations in surface affinities and/or collision rates could in principle lead to a deviation of the surface-measured distribution from the true solution distribution. We can, however, extract binding rates directly from our experimental data. For this, we employ standard flow cells(*33*) that exhibit large surface-to-volume ratios. As a result, binding to the surface reduces the analyte concentration throughout the experiment, as can be seen in Fig. 1D. We remark that this decay in sticking frequency cannot be attributed to surface saturation, because (a) we can add more sample to a flow chamber a few times and still observe binding, (b) for a 4×9 μm^2 field of view, a tightly packed monolayer of 5 nm diameter particles would contain $\sim1.8\times10^6$ particles, while we typically measure 10^3 binding events in an experiment, and (c) the lack of unbinding implies that we deplete the concentration in solution with time. The measured drop in binding frequency is well described by an exponential decay, consistent with a simple first-order process of protein molecules in solution binding to the glass surface with a given rate constant (Fig. S4A), which provides representative decay constants from multiple movies (Fig. S4B). Because we have sufficient mass resolution to distinguish different oligomeric states, we can characterise the decay in binding rate for each oligomeric state (Fig. S4C), measuring a rate constant which is a function of the surface sticking probability and the collision rate, which in turn is proportional to the diffusion coefficient.

The values of these rate constants for different oligomers and different species studied in this manuscript exhibit variations of less than ±25% from the mean decay for all oligomeric species per protein (Fig. S4C). For BSA, Env, smooth-muscle myosin and GroEL we observe a decrease in decay rate with molecular weight. For systems where we observe decay of a native, globular oligomeric structure into smaller subunits (ADH, β-amylase), the pattern is inverted. Importantly, the decay rates are highly reproducible with narrow standard deviations, demonstrating that they can be characterised with high accuracy on an oligomer-to-oligomer basis. We found excellent correlation between the absolute rate constant and the $(\text{molecular weight})^{-1/3}$, i.e. the scaling of the diffusion coefficient with mass assuming spherical objects,

suggesting that the surface affinity for different oligomeric states, and indeed different proteins, does not vary significantly (Fig. S4D).

To probe the effect of diffusion and surface attachment on oligomeric distributions and resulting thermodynamics parameters, we can apply a correction to the counted numbers of each oligomer depending on the measured binding rate constant. Assuming that any change in the equilibrium distribution as a result of this dilution is slow compared to the timescale of the experiment, then to accurately count the proportion of each oligomer present in solution, one would have to integrate over the exponential decay in binding events from the addition of sample (time, $t = 0$) until all binding has ceased. Experimentally, meanwhile, we effectively integrate from some time $t_0 \approx 15$ s after addition of sample up to a later time t_f when the acquired movie ends. We can relate these two via

$$N_i = M_i \frac{e^{k_i t_0}}{1 - e^{-k_i (t_f - t_0)}}$$

where N_i is the number of particles of oligomer i counted over the full integral, M_i is the number measured experimentally, and k_i is the binding rate constant for oligomer i.

As shown for BSA (Fig. S4E) corrections produce noticeable, but nevertheless small corrections to the mass distributions. While one might assume that the correction should lead to an increase in the dimer fraction because of compensation for diffusion, we find the opposite to be true. This is caused by the fact that we have to take into account the delay (t_0) between addition of the sample and observation of binding events, which is usually on the order of 15 s. During this time, a higher proportion of the smaller oligomers are lost to the surface, which leads to the measured correction factor. We observe similar effects for our Env-BanLec experiments (Fig. S4F), where the correction causes changes in the mole fractions that are within the error associated with our ability to model the experimental data.

We conclude that non-specific binding to microscope cover glass only weakly influences the oligomeric distributions determined by iSCAMS, suggesting that our measurements are representative of solution distributions, especially given the fact that they can be corrected by quantifying the probability of surface attachment and diffusion coefficient as a function of oligomeric state.

Accuracy, noise floor, resolution and precision

The mass deviation between sequence mass and measured mass according to a linear correlation from calibration proteins was <5 kDa. Comparison with molecular shape factor as extracted from structural data exhibited no clear correlation in magnitude or in sign (Fig. S6A). Therefore, at this stage we cannot quantitatively connect accuracy, mass and refractivity beyond a general rule that the accuracy is limited to a few kDa, which causes the percentage deviation to increase for smaller object mass as shown in the upper panel of Fig. 2A.

The noise floor of our approach, as defined by the standard deviation of background images recorded in the absence of biomolecules, decreases as expected for a shot noise-limited process for image averaging up to several tens of ms, after which it begins to deviate, with a minimum near 300 ms (Fig. S6B). We believe that the deviation is largely caused by sample drift, causing the surface roughness to begin to contribute to the ratiometric images. The noise floor represents the instrumental limit to mass resolution manifested in the width of the recorded mass distributions. In addition, we found that this width increases with mass (Fig. S6C), an effect that may be expected in the presence of an additional uncertainty that scales with size of the object measured. We currently believe that the source of this additional broadening is largely caused by the rough glass surface, which exhibits ±40% peak-to-peak variations in reflectivity in our experimental arrangement.

The theoretical precision, at least in the context of unimodal mass distributions is given by $\sigma/\sqrt{N}$, where σ is the standard deviation of the distribution and N the number of events measured. We find that this relationship frequently holds only for N<100, leading to a precision on the order of 2% of the object mass (see Fig. 2D). As above, we believe that the most likely limiting factors are the glass roughness and our ability to precisely determine the focus position from experiment to experiment in a repeatable fashion, inducing contrast and thus mass variations beyond the theoretical expectation.

Lipid nanodiscs preparation and procedure

Membrane scaffold proteins were expressed in *E.coli*, purified and assembled by addition of lipids in the molar ratios specified in Table S2, followed by purification by size exclusion chromatography as described previously(*38*). The nanodiscs were diluted to 10 nM in 20 mM Tris, 100 mM NaCl, pH 7.4, and nonspecific binding to a glass surface was measured according to the procedure described above. For comparison with expected masses for each sample, we took literature values (Table S3) for the mass of the MSP1D1 nanodisc with DMPC (1,2-

dimyristoyl-sn-glycero-3-phosphocholine), which we took as a reference, as measured by a variety of techniques to provide a range of expected masses. For each of these, including our own, we calculated an expected mass for the MSP1ΔH5 nanodisc with DMPC. This was done by subtracting the mass of the protein component and scaling the resulting mass of lipid by the reduction in area of the bilayer patch calculated from the square of the reduction in diameter of the nanodisc as measured by size exclusion chromatography (SEC), dynamic light scattering (DLS) and electron microscopy (EM) (*49*). The expected mass of the nanodisc follows by addition of the MSP1ΔH5 protein mass (Tables S3 and S4).

Similarly, for the MSP1D1 nanodiscs with varying lipid composition, we calculated a range of expected masses from the various reported measurements of the reference nanodisc. We scaled the measured lipid mass according to the expected changes due to different total number of lipid molecules per nanodisc (from the protein:lipid assembly ratio) and different average mass per lipid molecule. Again, addition of the mass of protein leads to the expected masses of the nanodiscs (Tables S5 and S6). The total number of detected particles were 14216 (MSP1D1-DMPC), 3041 (MSP1D1-DMPC/PC14:1/Chol), 2292 (MSP1D1-PC14:1/Chol), 2277 (MSP1Δ1-DMPC) from 2 − 12 experiments.

Env and BanLec preparation and procedure

Env SOSIP (BG505) and BanLec were prepared as described previously(*39*), either in the presence or absence of kifunensine. The proteins were each diluted to 5 nM in phosphate buffered saline (PBS) and binding to a glass surface was imaged in a flow chamber as described for the landing assay. The total number of detected particles were 15391 and 8048 for kifunensine-treated and wildtype Env, respectively.

For the interaction studies between Env and BanLec, Env was diluted to 20 nM in PBS. BanLec was diluted to 2-fold the working concentration in PBS. The protein dilutions were kept on ice until use. Env was mixed 1:1 with either PBS (as a control) or BanLec, and incubated for 5 min at room temperature. Next, 20 µl of the mixture were flushed into a PBS-filled flow chamber, and landing on the glass surface immediately recorded. The kernel density estimates of the probability densities shown in Fig. 3A were generated using a Gaussian kernel with bandwidth of 30 kDa. The number of each observed Env cluster was determined by counting landing events within resolvable contrast intervals, i.e. monomers, dimers, trimers, tetramers and above. In order to determine how many individual Env molecules were present in each

population, the number of landing events was multiplied with the respective number of Env units per oligomer (1 for monomeric Env, 2 for dimeric Env, 3 for trimeric Env, etc.). In this way, the fraction of Env molecules in clusters and relative abundance of the different species (Fig. 3B) could be calculated.

In order of increasing BanLec concentration, the total number of detected particles were: 4446, 4841, 3068, 3106, 6258, 3893, 7370, 4198, 3412, 3027, 3674, 4287, 3790.

Modelling of Env-BanLec interaction

We modeled the Env (A) BanLec (B) system as

$$A + A \rightleftharpoons A_2 \qquad K_d$$

$$A + B \rightleftharpoons AB \qquad K_{BanLec}$$

$$A_nB_n + A \rightleftharpoons A_{n+1}B_n \qquad K_{Env}$$

$$A_{n+1}B_n + B \rightleftharpoons A_{n+1}B_{n+1} \qquad K'_{BanLec}$$

From these equilibria, the concentration of each oligomer can be expressed in terms of a combination of equilibrium constants and powers of $[A]$ and $[B]$. Using the fact that the total number of each monomer is conserved, i.e.

$$[A]_0 = [A] + 2[A_2] + [AB] + \sum_{i=m}^{\infty} \sum_{n=m-1}^{m} m[A_mB_n]$$

$$[B]_0 = [B] + [AB] + \sum_{i=m}^{\infty} \sum_{n=m-1}^{m} n[A_mB_n]$$

where $[A]_0$ and $[B]_0$ are the initial concentrations, we thus obtained two simultaneous equations to solve (numerically) for $[A]$ and $[B]$ in terms of the equilibrium constants and the initial concentrations. Once $[A]$ and $[B]$ are known, the concentrations of all other species follow from the equilibrium conditions.

We obtained very good agreement with experiment for $K_{Env} \simeq 8$, $K_{BanLec} \simeq 0.4$, $K'_{BanLec} \simeq 0.12$, and $K_d \simeq 0.004$ all in units of $(\text{nM})^{-1}$. The initial concentration of Env in the calculation was taken to be 10 nM.

Supported Lipid Bilayer (SLB) preparation

CultureWell silicone gaskets (Grace Bio-Labs) were cut and placed onto a freshly cleaned coverslip providing four independent 30 − 50 µl sample chambers on the same substrate. Stock

solutions of 1,2-dioleoyl-sn-glycero-3-phosphocholine (DOPC) and 1,2-dioleoyl-sn-glycero-3-phospho-L-serine (DOPS) in chloroform were purchased from Avanti Polar Lipids (Alabaster, AL). The DOPC:DOPS (3:1) mixture was dried to a film, kept under vacuum for at least 1 h and brought to a concentration of 1 mg ml^{-1} in bilayer buffer (10 mM HEPES, pH 6.8, 200 mM NaCl, 2 mM $CaCl_2$). Using a mini-extruder (Avanti Polar Lipids), the suspension was then forced 21 times through a single membrane with a pore size of 100 nm. SLBs were formed by vesicle fusion inside the chamber on cleaned coverslips that have been passed through a blue flame. After 5 − 10 min incubation, excess vesicles were removed from the chamber by rinsing with 10 mM sodium phosphate buffer, pH 7.0.

α-Synuclein preparation

The construct was expressed and purified as described previously(*40*), lyophilized and stored at −20 °C. The lyophilized protein was dissolved at a final concentration of 1−1.5 mM in 20 mM sodium phosphate, pH 7.0. In order to allow complete dissolution of the protein powder, the pH of the α-synuclein solution was adjusted to 7.0 with 1 M sodium hydroxide.

α-Synuclein aggregation imaging and analysis

Before addition to the SLBs the protein was diluted in sodium phosphate buffer. 10 µl of α -synuclein solution added to a sample volume of 30 µl, yielding the final reported concentrations. Addition of α-synuclein was recorded at 100 frames/s and aggregate formation was followed for 20 s. The acquired images consisted of 512×512 $pixels^2$ with a pixel size of 23.4 nm/pixel, resulting in a field of view of 12×12 μm^2. As with the protein binding assays, these images were 3×3 pixel-binned before additional processing, giving a final pixel size of 70.2 nm/pixel. To capture the initial growth, the entire image stack was divided by a background image. The background was chosen as the average of frames before addition of α-synuclein, which can be observed as a brief disturbance during Movie S2. After selecting an 11×11 $pixel^2$ region of interest centred on each growing aggregate, we fitted this region in each frame to the difference-of-two-Gaussians model function, as described for the analysis of protein landing events. The contrast was plotted as a function of time, and the initial growth rate was determined by a linear fit for 0.1 − 1 s of data after addition of α -synuclein, depending on concentration.

Preparation of biotin-PEG flow chambers for actin polymerization assays

Microscope cover glass (No. 1.5, 24 × 50 mm^2, VWR) was sonicated sequentially in 2% Hellmanex, H_2O and ethanol each for 10 min, then 0.1 M KOH for 15 min and finally 5 min in

H_2O. In between each step, they were washed with H_2O to remove excess solution from the previous step. All coverslips were individually rinsed with H_2O and ethanol, then blow-dried with a clean stream of nitrogen. A solution of 2 mg ml^{-1} mPEG-silane (MW 2000, LaysanBio) and 0.1 mg ml^{-1} biotin-PEG-silane (MW 3400, LaysanBio) in 80% ethanol at pH 2.0 (adjusted with HCl) was prepared immediately before being sandwiched between two cleaned coverslips. The sandwiches were incubated in petri-dishes at 70 °C for 16 h. The biotinylated coverslips were vigorously rinsed with H_2O and ethanol in an alternating fashion removing any dried excess PEG, then blow-dried with a clean stream of nitrogen. Small coverslips (No. 1.5, 24 × 24 mm^2, VWR) were rinsed with H_2O and ethanol in an alternating fashion and blow-dried with nitrogen. Flow chambers were assembled as described above. The flow chambers were stored in a dry nitrogen atmosphere at −20 °C.

Actin *in vitro* polymerization

Rabbit skeletal muscle actin was purified as described previously(*41*). Biotinylated actin was purchased from Cytoskeleton Inc. (Denver, USA, Cat. no. AB07-A). Avidin (Cat. no. A9275) was purchased from Sigma Aldrich. A biotin-PEG flow chamber was filled with G-actin buffer (2 mM Tris-HCl, 0.2 mM $CaCl_2$, pH 8.0), flushed with 40 µl of 10 µg ml^{-1} avidin in G-actin buffer and incubated for 5 min. Excess avidin was flushed out with 40 µl of G-actin buffer. Immediately before addition to the flow chamber, polymerization of a mixture of G-actin and 1% biotinylated G-actin (final concentrations: 300 − 1000 nM actin, 3 − 10 nM biotin-actin) in G-actin buffer containing 0.2 mM ATP and 2 mM DTT was induced by adding 1/10 of a volume of 10× KMEH buffer (1× concentration: 10 mM HEPES, 50 mM KCl, 2 mM $MgCl_2$, 1 mM EGTA, pH 7.4). A volume of 50 µl of the polymerization mixture was flowed into the chamber. A 9 × 9 $µm^2$ field of view was recorded at 468 frames/s.

Actin polymerization data analysis procedure

The movies of actin polymerization were analyzed using custom software written in LabVIEW. The raw video was 2×2 pixel-binned, resulting in an effective pixel size of 46.8 nm/pixel. To visualize the actin filaments on top of the signal from the glass surface roughness, a background image was created by taking a median of 20 raw images, and used to background-correct subsequent frames. To reduce shot noise, 8 consecutive frames were averaged, which gave an effective frame rate of 58.5 Hz. Actin filament tips were tracked by selecting a region of interest that included only the tip to be analyzed. Each frame of this region was then fit using a

filament tip model function(*42*), consisting of a Gaussian wall $w(x, y)$ starting at x_0 and y_0 running in direction θ with width σ:

$$w(x,y) = exp\left[-\frac{\left((x-x_0)\sin\theta + (y-y_0)\cos\theta\right)^2}{2\sigma^2}\right]$$

which is attached to half of a symmetric 2D Gaussian $g(x, y)$ having its centre at x_0 and y_0 with width σ

$$g(x,y) = exp\left[-\frac{(x-x_0)^2 + (y-y_0)^2}{2\sigma^2}\right]$$

The two functions are attached to each other by defining the border $b(x, y)$ between them in the following manner:

$$f(x,y) = (y-y_0)\cos\left(\theta - \frac{\pi}{2}\right) - (x-x_0)\sin\left(\theta - \frac{\pi}{2}\right) + 0.5$$

$$b(x,y) = \begin{cases} 0, f(x,y) < 0 \\ f(x,y), 0 \le f(x,y) \le 1 \\ 1, f(x,y) > 1 \end{cases}$$

The tip function $t(x,y)$ with an amplitude A is then created as:

$$t(x,y) = A\left[b(x,y)g(x,y) + \left(1 - b(x,y)\right)w(x,y)\right]$$

A LabVIEW representation of this function was fitted to the filament tip images using the Levenberg-Marquardt algorithm. The filament tip position was defined by the best fit values for x_0 and y_0. The trajectories were rotated such that the growth axis was aligned with the x-axis of the coordinate system. Step traces as shown in Fig. 4D were created by plotting the *x*-axis position *vs.* time.

Steps were automatically detected by a LabVIEW implementation of a previously described step finding algorithm (*43*, *44*). Briefly, we describe the step traces as a sequence of values, x_1, x_2, …, x_n, which are drawn from an unknown number of normal distributions of equal variance (σ^2) but different means (μ). The algorithm then searches for the change points of μ, i.e. step positions, in the data series, one at a time. This is done by segmenting the sequence at each position $k = 1, \ldots, n–1$ and testing the null hypothesis

$$H_0: \mu_1 = \mu_2 = \cdots = \mu_n$$

against the alternative

$$H_1: \mu_1 = \cdots = \mu_{k_0} \neq \mu_{k_0+1} = \cdots = \mu_n$$

where $1 < k_0 < n$ is the unknown position of a change point. Once a change point is found the sequence is divided into two sequences before and after the accepted change point. For each sequence the process is repeated until no more change points are found, i.e. the null hypothesis is accepted. Hypothesis testing was performed based on the principle of minimization of the Schwarz information criterion (*SIC*), defined by

$$SIC = p\log n - 2\log L(\theta)$$

where $L(\theta)$ is the maximum likelihood function for the model, p is the number of free parameters in the model, and n is the sample size. With $SIC(n)$ being the *SIC* under H_0, and $SIC(k)$ being the *SIC* under H_1, for a change point at a position $k = 2, ..., n-2$. The hypothesis H_0 is accepted if $SIC(n) \leq \min_k SIC(k)$, otherwise H_0 is rejected if there is a k for which $SIC(n) > SIC(k)$. The change point position is chosen to be where $SIC(k)$ is smallest in the data sequence. For our case, assuming a shifting mean and a constant variance, the two SIC values are obtained as

$$SIC(n) = n\log 2\pi + n\log \sigma^2 + n + 2\log n$$

$$SIC(k) = n\log 2\pi + k\log \sigma_1^2 + (n-k)\log \sigma_n^2 + n + 3\log n$$

where $\sigma^2 = \frac{1}{n}\sum_{i=1}^{n}(x_i - \bar{x})^2$, $\sigma_1^2 = \frac{1}{k}\sum_{i=1}^{k}(x_i - \bar{x})^2$, and $\sigma_n^2 = \frac{1}{n-k}\sum_{i=k+1}^{n}(x_i - \bar{x})^2$. Since this method works solely based on comparison of the *SIC* values, it does not require any input other than the data sequence and finds steps without user bias. We only included change points that are at least three data points apart from another, in order to eliminate steps that are found based on large fluctuations on a very short timescale. We emphasize that changing the minimum delay had a negligible effect on the obtained step sizes (Fig. S10E,F). The distribution of step sizes was described by a Gaussian mixture model using the expectation maximization algorithm in MATLAB. Errors of the fitting parameters were estimated using a bootstrap procedure with 1000 bootstrap samples.

Phalloidin-actin control experiment

We attempted a control experiment with static actin filaments to provide a baseline in terms of filament end tracking and to determine whether any end displacements could result from the

entire filament moving across the surface. Unfortunately for this experiment, actin filaments are generally dynamic at their ends and the absence of G-actin in solution causes their depolymerisation. G-actin at the critical concentration causes no net growth, but subunits will exchange at the filament tips. To minimize this effect, we used the actin filament stabilizer phalloidin. A mixture of 10 μM G-actin and 0.1 μM biotin-G-actin in G-actin buffer containing 0.2 mM ATP and 2 mM DTT was polymerized for 1 h at room temperature by adding 1/10 of the volume of 10× KMEH. It was then diluted 5-fold in 1× KMEH and mixed with 3 μM phalloidin (Sigma P2141) in 1× KMEH. The filaments and phalloidin were incubated overnight at 4 °C. On the day of the experiment, the phalloidin-stabilized filaments were diluted to 100 nM in 1× KMEH and kept on ice until use. The biotin-avidin-flow chambers were prepared as described above, then 30 μl phalloidin-actin were added. The attachment of filaments was monitored under similar imaging conditions as the polymerization experiments.

The presence of phalloidin markedly reduced any dynamics at the filament tips, but did not fully stop them at our levels of sensitivity. We could, however, correlate the displacements of the two ends of individual filaments in order to rule out that any tip position fluctuations are caused by an overall movement of the filaments. We selected 9 short phalloidin-stabilized filaments whose two tips were both visible and isolated from other filaments (Fig. S10A). We tracked both tips and determined their displacements along the filament axis as described above, orienting the resulting trajectories such that the two tips were facing opposite directions. We found no correlation between the displacements of the two tips on the same filament (Fig. S10B) suggesting that length fluctuations at the two filament ends are not caused by movement of the filament.

Actin filament growth simulation

To test the fidelity of our step finding algorithm, custom written software in LabVIEW created movies of growing actin tips. The model function described in the actin polymerization data analysis procedure section was used to generate actin filament tips with amplitude $A = -0.06$ and width $\sigma = 1.7$ pixels in a 15×15 pixel^2 image, which is similar to the experimental values assuming a pixel size of 46.8 nm. The experimental shot noise level was determined by dividing the respective pixel values of one frame in the experimental videos (averaged to 58.5 Hz) by those of the previous frame and determining the standard deviation of the pixel values in the resulting differential images. The LabVIEW Gaussian noise generator was used to produce

images with the experimental shot noise level (1.8×10^{-3}), which was then added to the filament tip images. The length of the actin filament tip was extended or shortened in consecutive frames by moving the tip position a defined distance (here 1, 2, 2.7, 4, 5 or 8 nm) forward or backward along the filament axis.

The dwell times of the tip between forward steps or backward steps were randomly chosen from two pools of exponentially distributed dwell times generated according to $T = -\ln U/k$, where T is the dwell time, U a uniformly distributed random number between 0 and 1, and k the rate constant. The rate constant for subunit attachment (forward step) k_1 was 4.887 s^{-1} and the rate for subunit detachment (backward step) k_{-1} was 2.103 s^{-1}, both based on experimentally determined kinetics (Fig. S10C at 0.3 μM). The dwell times were used to create a sequence of attachment and detachment events, which were treated independently, for a time period of at least the length of the simulated video. For a simulated video of 15 s at 58.5 Hz frame rate the program checks each frame whether an event is due according to the sequence of events generated before and either executes the event or leaves the filament unchanged. Multiple events happening during one frame time is possible and accounted for. The simulated image sequences are analyzed in the same way as the experimental videos as described in the actin polymerization data analysis procedure section. The simulation with 2.7 nm step size matches our step size histogram in Figure 4E well, with smaller steps detectable, albeit returning a larger than defined step size (Fig. S10D). Overall, these simulations demonstrate that the assumption-free step-detection algorithm is capable of robustly identifying and quantifying 2.7 nm given the experimental noise level.

Determination of actin macroscopic growth rates

A smoothing spline was fitted to the 2D trajectories obtained from tracking actin filament tips, as in the actin polymerization data analysis procedure section. The length of this spline was used as the average tip displacement d. The average elongation velocity v of the filament tip was calculated according to

$$v = \frac{d \times F_r}{n}$$

where F_r is the frame rate and n the number of frames, leading to the average elongation rate

$$r = \frac{v}{A_s}$$

where A_S is the actin subunit size, assumed to be 2.7 nm(*45*). This procedure was repeated for a number of actin filaments growing at different actin concentrations. The elongation rate as a function of actin concentration can be described by

$$r = k_{+1}[actin] - k_{-1}$$

where k_{+1} is the subunit association rate constant, k_{-1} is the subunit dissociation constant and $K_{crit} = k_{-1}/k_{+1}$ is the critical concentration for actin polymerization(*46*). The critical concentration (129 ± 151 nM) and rate constants (k_{+1} = 16.3 ± 5.0 μM^{-1} s^{-1} and k_{-1} = 2.1 ± 2.4 s^{-1}) obtained from Fig. S10C agrees well with previous studies(*47*).

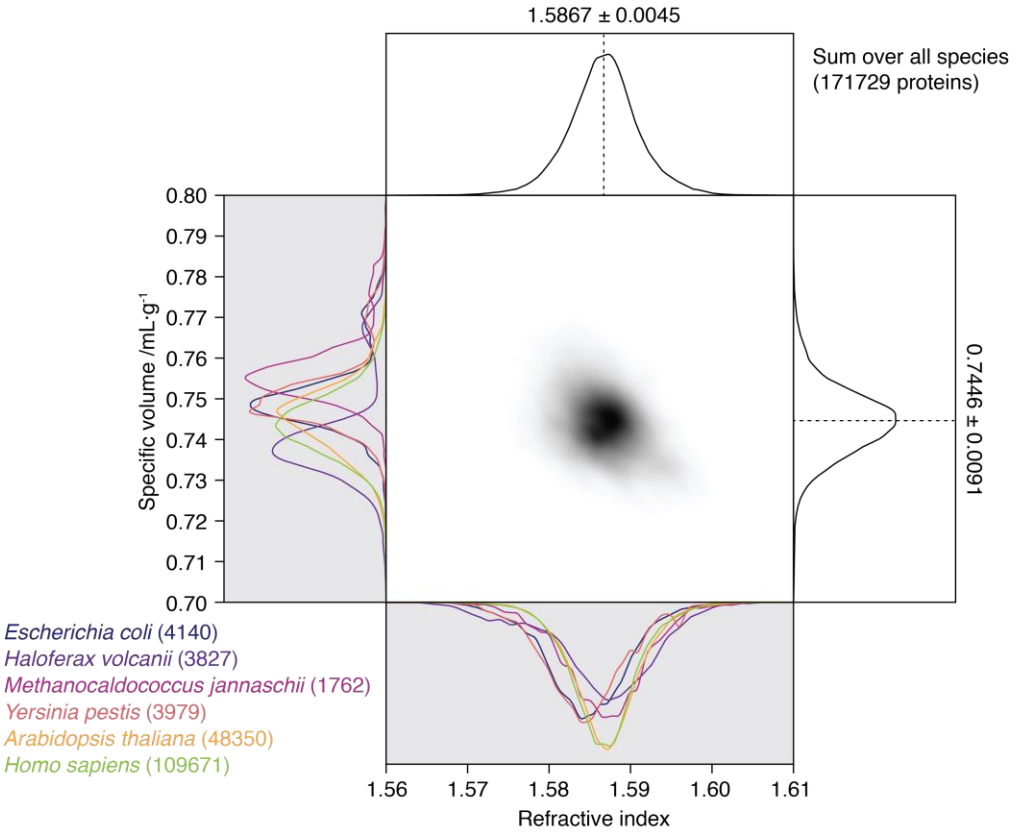

Fig. S1.

One-dimensional distributions of refractive index (top, bottom) and specific volume (left, right) for all proteins in six genomes, as calculated from the amino acid sequences, and the two-dimensional distribution of both quantities (middle). The top, right, and middle panels show the combined data from all genomes. The left and bottom panels show the respective distributions for the separate genomes, renormalized to have identical areas.

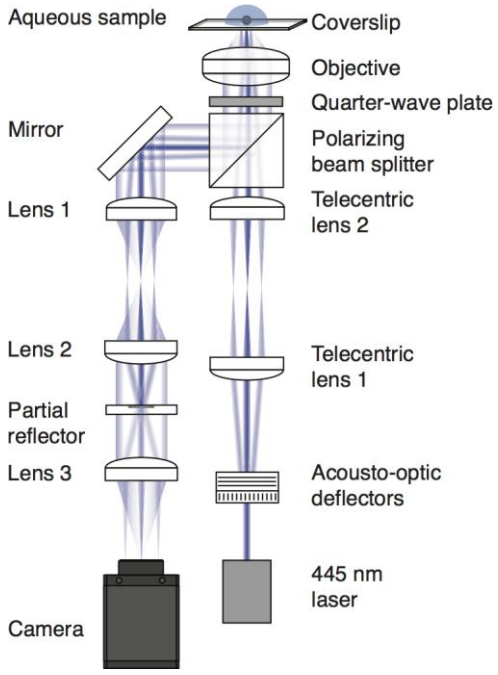

Fig. S2.

Schematic of the experimental setup.

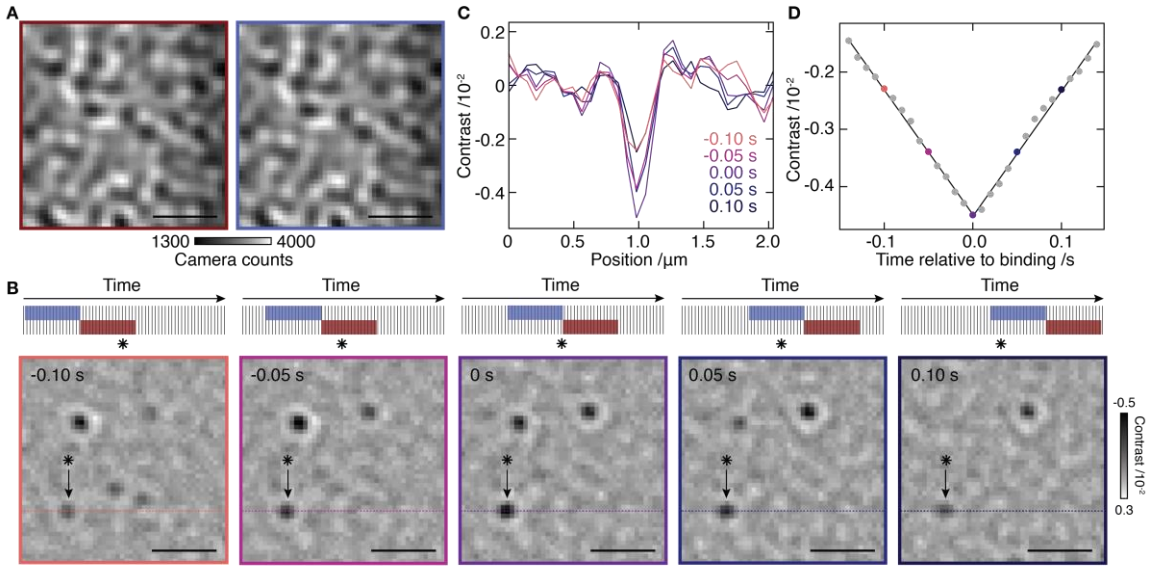

Fig. S3.

Data analysis. (**A**) Raw camera images before and after the landing event in **B-D** showing image contrast due to coverslip roughness. (**B**) Illustration of the image averaging and differential imaging approach. The asterisk marks a landing event. Individual images are averaged into two consecutive blocks (blue and red), which are normalized and divided to provide differential contrast. The mid-point is scanned in time, meaning that the signal from stochastic landing events grows and fades, as indicated by the black arrow. Scale bars: 1 µm. (**C**) Corresponding cross-sections for the particle highlighted in **B**. (**D**) Corresponding signal magnitudes extracted by a fit to the PSF and fit (black).

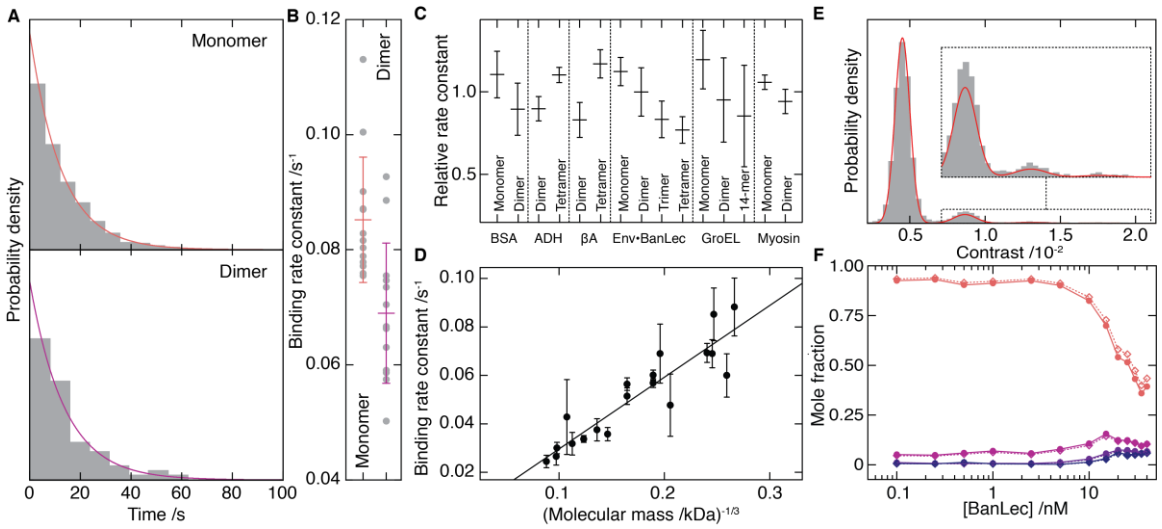

Fig. S4.

Solution vs surface mass distributions. (**A**) Changes in binding time distributions for BSA monomers and dimers from the same data as shown in Fig. 1 and corresponding exponential fits. (**B**) Resulting binding rate constants for 11 different movies. (**C**) Binding constants for a variety of proteins exhibiting more than one oligomeric state studied in this work, normalized to the average binding constant for each protein. (**D**) Plot of binding constant vs (molecular weight)$^{-1/3}$, except for those exhibiting inverted behavior but including protein samples exhibiting only a single oligomeric state as well as those in **C**, together with a linear fit describing the behavior expected from diffusion scaling. (**E**) BSA mass distribution before (solid bars) and after (red line) scaling for mass-dependent diffusion. (**F**) Env-BanLec oligomeric evolution before (solid) and after (dashed) correction for surface effects.

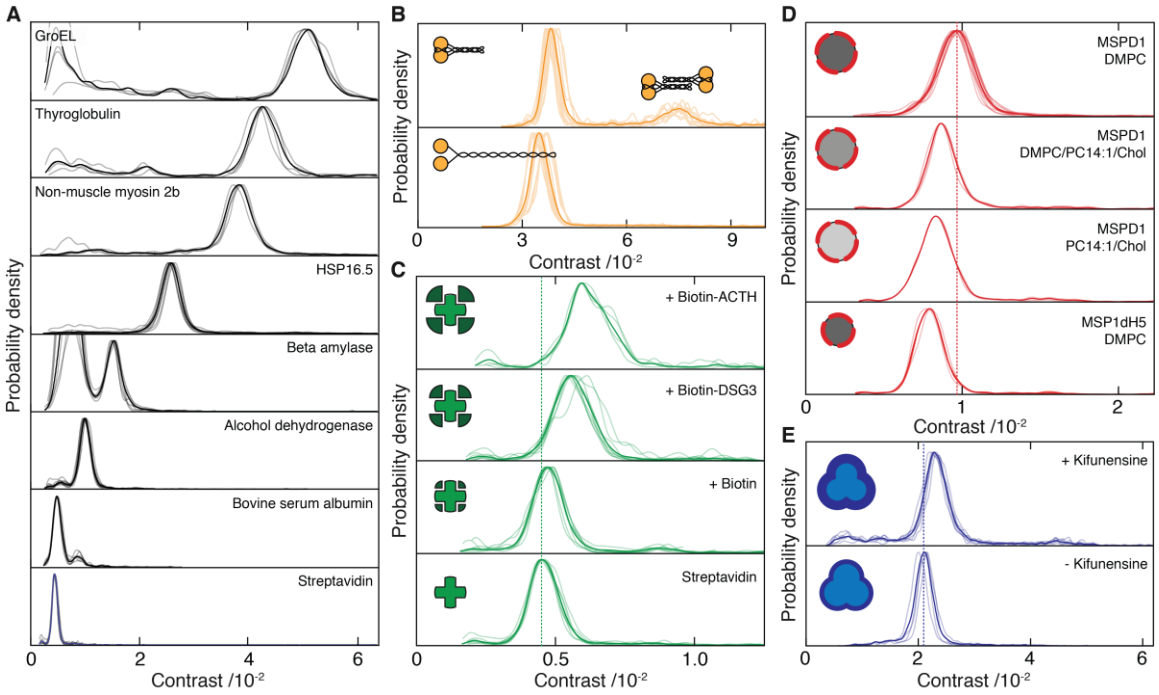

Fig. S5.

Kernel densities for Fig.2 in the main manuscript. (**A**) Calibration proteins: GroEL 14mer (802.6 kDa), thyroglobulin (669 kDa), non-muscle myosin 2b (597 kDa), HSP16.5 24mer (394.8 kDa), β-amylase (224.3 kDa) showing some dissociation at the low concentrations at which we measured, alcohol dehydrogenase (147.4 kDa), BSA (66.4 kDa), streptavidin (52.8 kDa). (**B**) Smooth-muscle myosin. (**C**) Biotin-streptavidin. (**D**) Lipid nanodiscs. (E) Env expressed in the presence and absence of kifunensine. The Kernel bandwidths were 3, 5, 5, 7.5, 10, 10, 12 and 15 kDa with increasing mass for **A**; 9 kDa for **B**; 3 kDa for **C**; 5 kDa for **D**; 10 kDa for **E**.

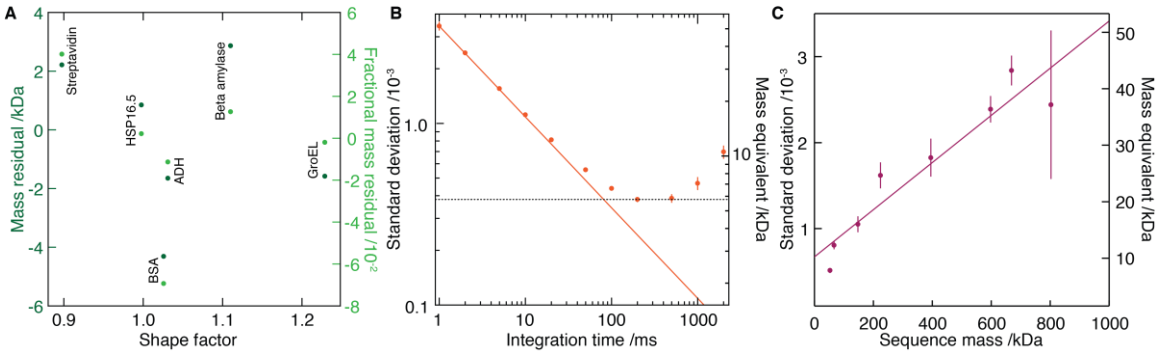

Fig. S6.

Noise, resolution and shape-dependence characterization. (**A**) Absolute and fractional mass residuals as a function of molecular shape factor(*48*). (**B**) Standard deviation of differential images as a function of integration time, for acquisition at 1000 frames/s. The dashed line indicates the nominal noise floor, and the solid line expectation based on shot noise. (**C**) Standard deviation of contrast histograms obtained for the 8 calibration proteins from Fig. 2A, including a linear fit as a guide to the eye

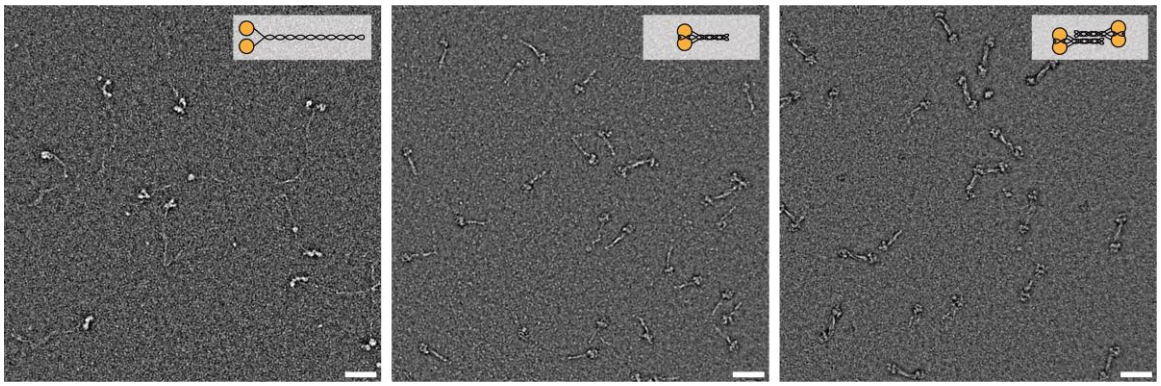

Fig. S7.

EM images of SMM in the extended (6S, left) and folded (10S, middle) conformation. Cross-linking at 25 mM salt increased the fraction of SMM dimers (right). Scale bar: 50 nm.

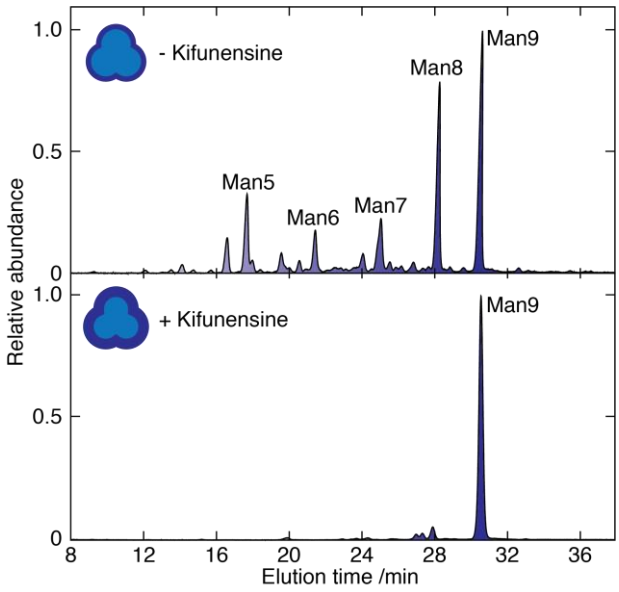

Fig. S8.

High-performance liquid chromatography of N-glycans released from Env expressed in the absence (top) and presence (bottom) of kifunensine. The corresponding average masses are determined to be 1664 and 1885 Da, respectively, based on peak height.

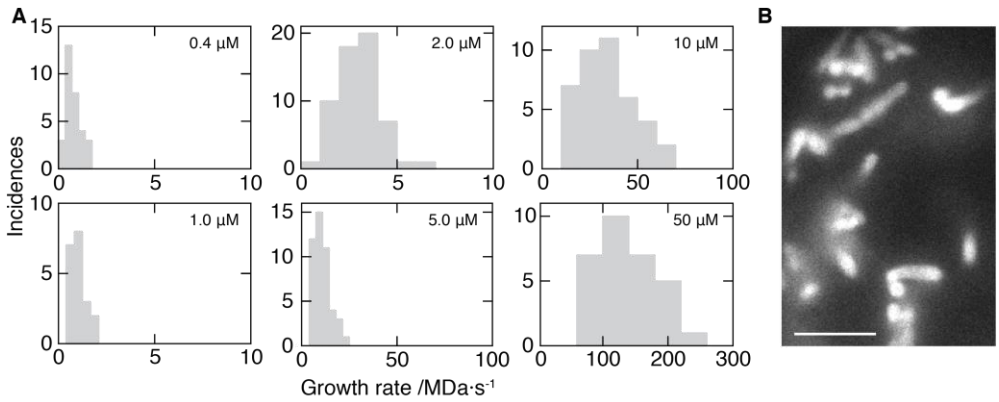

Fig. S9.

Initial growth rate distributions, and thioflavin-T staining for α-synuclein aggregation. (**A**) Growth rate histograms underpinning Fig. 4B from the main text. Total number of particles analyzed: 31, 20, 58, 46, 40, 30. (**B**) Fluorescence image after thioflavin- T staining of a bilayer aggregation assay at 10 µM after overnight incubation. Scale bar: 5 µm.

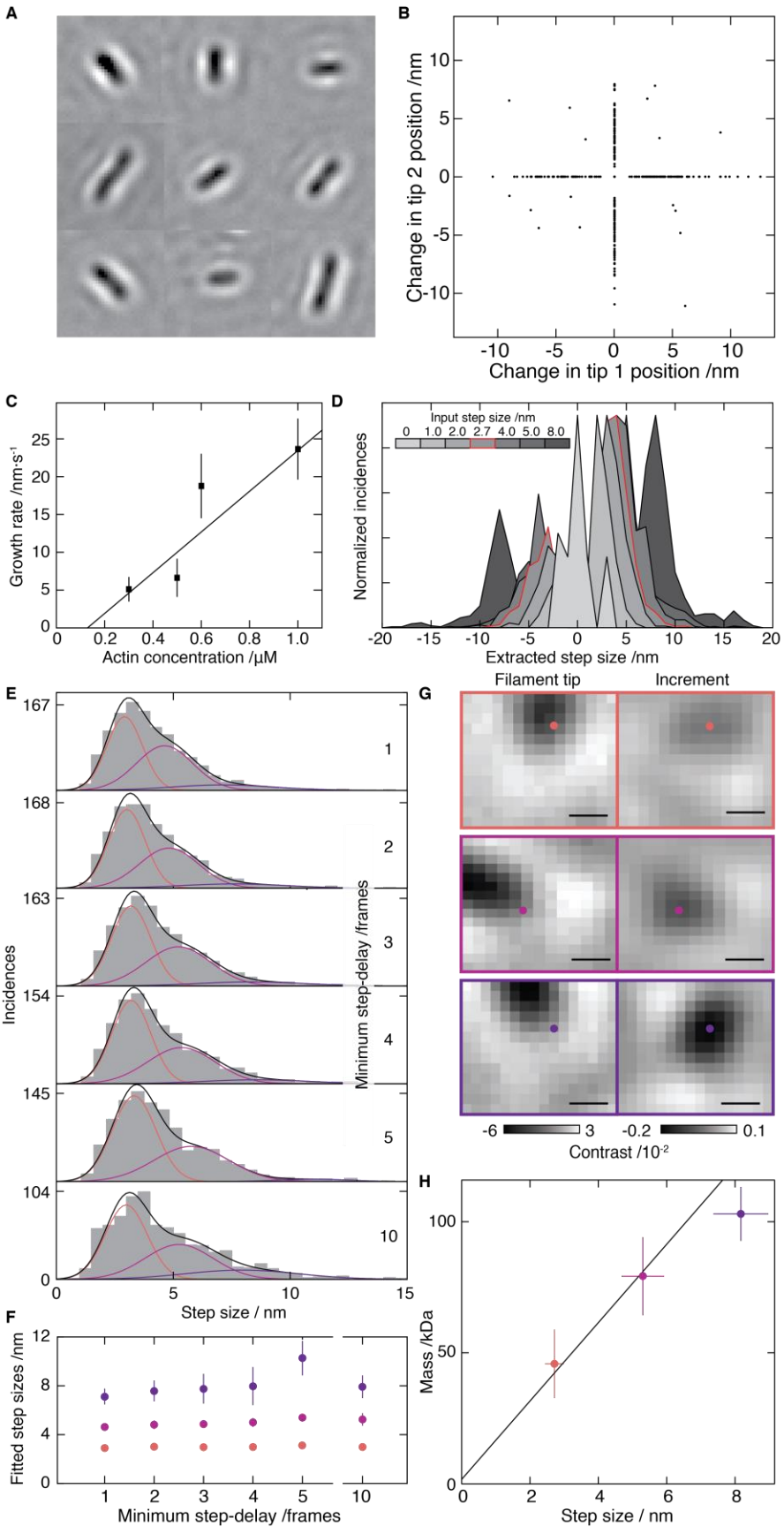
A
B
Change in tip 2 position /nm
Change in tip 1 position /nm
C
Growth rate /nm·s⁻¹
Actin concentration /μM
D
Input step size /nm
0 1.0 2.0 2.7 4.0 5.0 8.0
Normalized incidences
Extracted step size /nm
E
Incidences
Minimum step-delay /frames
Step size / nm
F
Fitted step sizes /nm
Minimum step-delay /frames
G
Filament tip
Increment
Contrast /10⁻²
H
Mass /kDa
Step size / nm

Fig. S10.

Addition of actin to individual filaments. (**A**) Representative 1.7×1.7 μm^2 images of short phalloidin-stabilized actin filaments. (**B**) Scatter plot of detected steps at the two ends of the filament for the filaments from **A**. (**C**) Macroscopic growth rate recorded for 26, 14, 37 and 10 different filaments at increasing actin concentration including a linear fit. (**D**) Step size histograms resulting from applying the step-finding algorithm to simulated step traces with different step sizes. In each case, 16 filaments were simulated with a total number of 1500 steps. The total number of detected steps were 22, 301, 575, 704, 940, 1088 and 1247 for 0-8 nm steps. (**E**) Experimental step size distributions as a function of minimum delay time between steps including fits to a Gaussian mixture model. (**F**) Step sizes determined from **E**. (**G**) Representative images of the growing filament (left) and differential mass image (right) for 2.8, 5.6 and 8.4 nm steps. The points indicate the centre of the differential mass and are overlaid on the image of the filament tip. Scale bar: 200 nm. (**H**) Mass corresponding to 1,2 and 3 subunit additions obtained from images such as those shown in **G**, using 11, 14 and 8 events, respectively. The line indicates a linear fit to 0, 1 and 2 subunit additions to obtain a step size-to-mass conversion.

Table S1.

Contributions to R, V_i, and M_i for the canonical amino acids.

Amino acid	n_{aa} /g	V_i /(cm^3 /mol)	M_i /Da
A	0.242	54.26723	89.0932
R	0.253	116.12344	174.201
N	0.229	76.79325	132.1179
D	0.227	70.52933	133.1027
C	0.238	62.33805	121.1582
Q	0.237	89.98362	146.1445
E	0.233	84.80384	147.1293
G	0.225	38.42674	75.0666
H	0.253	95.94639	155.1546
I	0.282	99.31927	131.1729
L	0.279	99.13858	131.1729
K	0.266	102.391	146.1876
M	0.263	101.00571	149.2113
F	0.287	116.54505	165.1891
P	0.245	74.14313	115.1305
S	0.22	56.73666	105.0926
T	0.236	72.276	119.1192
W	0.297	139.55291	204.2252
Y	0.272	118.71333	181.1885
V	0.27	83.77993	117.1463

Table S2.

Composition key (all with MSP1D1 as the scaffold protein). *MSP1D1/DMPC nanodisc taken as reference for size comparison.

Composition	Lipid	Percentage	Mass/ Da	Average Lipid Mass /Da	Protein:lipid assembly ratio	Relative mass of lipid content
a*	DMPC	100	677.9	677.9	1:80	1
b	DMPC PC14:1 Cholesterol	40 50 10	646.8 645.2 386.7	646.8	1:73.5	0.877
c	PC14:1 Cholesterol	90 10	673.9 386.7	645.2	1:67	0.797

Table S3.

Reduction in total mass of nanodisc calculated for a range of measured masses of the MSP1D1 DMPC nanodisc. All values are given in kDa. SEC, DLS and NMR data are from (*49*) and native MS from (*50*).

MSP1D1 mass	Technique	MSP1D1 lipid mass	Exp. MSP1ΔH5 lipid mass			Exp. MSP1ΔH5 nanodisc mass		
			SEC	DLS	EM	SEC	DLS	EM
141.0	iSCAMS	93.9	74.6	72.9	67.4	116.6	114.9	109.4
124.0	SEC	76.9	61.1	59.7	55.2	103.1	101.7	97.2
126.0	DLS	78.9	62.7	61.2	56.6	104.7	103.2	98.6
149.5	Native MS	102.4	81.4	79.5	73.5	123.3	121.5	115.5
158.0	NMR	110.9	88.1	86.1	79.6	130.1	128.1	121.6

Table S4.

Size comparison for lipid nanodiscs. Reduction in area of lipid bilayer patch in nanodisc with reduction in size of scaffold protein, calculated from reduction in hydrodynamic diameter as measured by SEC, DLS or EM (*49*). D = diameter, R_{lo} = radius of lipid-only content assuming the belt protein contributes 0.5 nm to the radius.

Technique	MSP1D1		MSP1ΔH5		Ratio of lipid areas: MSP1ΔH5/MSP1D1
	D/nm	R_{lo} /nm	D/nm	R_{lo} /nm	
SEC	10.2	4.6	9.2	4.1	0.79
DLS	9.4	4.2	8.4	3.7	0.78
EM	9.5	4.25	8.2	3.6	0.72

Table S5.

Composition b predictions. All values are given in kDa.

Mass of MSP1D1	Lipid mass in MSP1D1 nanodisc	Expected lipid mass	Expected nanodisc mass
141.0	93.9	82.3	129.4
124.0	76.9	67.4	114.5
126.0	78.9	69.2	116.3
149.5	102.4	89.8	136.9
158.0	110.9	97.2	144.3

Table S6.

Composition c predictions. All values are given in kDa.

Mass of MSP1D1	Lipid mass in MSP1D1 nanodisc	Expected lipid mass	Expected nanodisc mass
141.0	93.9	74.9	121.9
124.0	76.9	61.3	108.4
126.0	78.9	62.9	110.0
149.5	102.4	81.6	128.7
158.0	110.9	88.4	135.5

Table S7.

Contrast-mass conversions (linear fit parameters to a contrast vs mass calibration plot as shown in Fig 2A) for all data shown in Fig 2. The different datasets were taken at different times, and as a result of the use of partial reflectors of different transmissivity, oxidation of the partial reflector, and minor drifts in alignment, the values for converting between mass and contrast were different over time. The setup was calibrated for each measurement using the procedure outlined for Fig. 2A, and for ease and consistency of display the contrasts shown for each measurement in Figs. 2 and S5 were normalized to the contrast as in Fig. 1.

Figures	Description	Slope /kDa^{-1}	Intercept
1, 2B, S5C	BSA; streptavidin-biotin binding,	6.5651E-05	4.2324E-04
2A, S5A	Representative Calibration	2.0529E-05	3.3099E-04
2C, S5D	Lipid nanodiscs	1.6483E-05	0.0000E+00
2D, S5E	Env +/- kifunensine comparison	1.5410E-05	0.0000E+00

Table S8.

Abbreviations used in Fig. 2. *Exact sequences given on page S4.

Abbreviation	Meaning	Description
SEC	size-exclusion chromatography	Experimental techniques used in the literature for mass determination of the MSP1D1/DMPC nanodisc
DLS	dynamic light scattering	
MS	(native) mass spectrometry	
NMR	nuclear magnetic resonance	
MSP1D1	Membrane scaffold protein (MSP) 1 with the first 11 N-terminal amino acids removed, as described in (*51*)	Membrane scaffold proteins (MSPs) used to make the lipid nanodiscs
MSP1ΔH5	MSP1D1 with the 5th α-helix deleted, as described in (*49*)	
DMPC	1,2-dimyristoyl-*sn*-glycero-3-phosphocholine	Lipids used in the lipid nanodiscs
PC14:1	1,2-dimyristoleoyl-*sn*-glycero-3-phosphocholine	
Chol	cholesterol	
DSG3	desmoglein-3	Biotinylated peptides in Fig 2D*
ACTH	adrenocorticotropic hormone	

Movie S1

First 30 s (real time) of a representative ratiometric movie of BSA molecules binding non-specifically to a glass coverslip. The field of view is 3.2 x 9.7 μm^2, and the contrast scale is from -0.0075 to +0.003. The raw frames were saved at 100 Hz, and the sliding ratiometric processing was applied with a frame averaging of 5 frames. The movie is played back at 30 Hz.

Movie S2

Representative background-divided movie of addition of 1 μM α-synuclein to a supported lipid bilayer, showing the initial perturbation of the sample due to manual addition of the α-synuclein followed by growth of aggregates on the bilayer. The field of view is 11.9 x 11.9 μm^2, and the contrast scale is from -0.12 to +0.08. The frames were recorded at 100 Hz, and are played back at 33 Hz.

Movie S3

500 nM actin (+1% biotin-actin) polymerizing on avidin-biotin-PEG-coated glass. The size is 3.1 x 4.4 μm^2 (scale bar = 1 μm), and the contrast scale is from -0.05 to +0.04. Images were recorded at 468 Hz then averaged to 3 Hz, and are played back at 25 Hz.

Movie S4

Growing actin filament tips corresponding to the traces shown in Fig. 4D. The actin concentration was 300 nM, the scale bar is 250 nm, and the contrast scale is from -0.05 to +0.04. Images were recorded at 468 Hz then averaged to 58.5 Hz (as for the analysis performed for Fig. 4D), and are played in real time.

Supplementary references

31. T. L. McMeekin, M. L. Groves, M. Wilensky, Refractive Indices of Proteins in Relation to Amino Acid Composition and Specific Volume. *Biochem. Biophys. Res. Commun.* **7**, 151–156 (1962).

32. Y. Harpaz, M. Gerstein, C. Chothia, Volume Changes on Protein-Folding. *Structure*. **2**, 641–649 (1994).

33. A. Yildiz *et al.*, Myosin V walks hand-over-hand: Single fluorophore imaging with 1.5-nm localization. *Science*. **300**, 2061–2065 (2003).

34. N. Billington, A. Wang, J. Mao, R. S. Adelstein, J. R. Sellers, Characterization of Three Full-length Human Nonmuscle Myosin II Paralogs. *J. Biol. Chem.* **288**, 33398–33410 (2013).

35. J. R. Sellers, M. D. Pato, R. S. Adelstein, Reversible Phosphorylation of Smooth-Muscle Myosin, Heavy-Meromyosin, and Platelet Myosin. *J. Biol. Chem.* **256**, 3137–3142 (1981).

36. L. Yang *et al.*, An adaptive non-local means filter for denoising live-cell images and improving particle detection. *J. Struct. Biol.* **172**, 233–243 (2010).

37. M. S. Woody, J. H. Lewis, M. J. Greenberg, Y. E. Goldman, E. M. Ostap, MEMLET: An Easy-to-Use Tool for Data Fitting and Model Comparison Using Maximum-Likelihood Estimation. *Biophys. J.* **111**, 273–282 (2016).

38. C. Tzitzilonis, C. Eichmann, I. Maslennikov, S. Choe, R. Riek, Detergent/Nanodisc Screening for High-Resolution NMR Studies of an Integral Membrane Protein Containing a Cytoplasmic Domain. *PLoS ONE*. **8**, e54378 (2013).

39. R. W. Sanders *et al.*, A Next-Generation Cleaved, Soluble HIV-1 Env Trimer, BG505 SOSIP.664 gp140, Expresses Multiple Epitopes for Broadly Neutralizing but Not Non-Neutralizing Antibodies. *Plos Pathogens*. **9**, e1003618 (2013).

40. S. Campioni *et al.*, The Presence of an Air-Water Interface Affects Formation and Elongation of alpha-Synuclein Fibrils. *J. Am. Chem. Soc.* **136**, 2866–2875 (2014).

41. S. S. Lehrer, G. Kerwar, Intrinsic Fluorescence of Actin. *Biochemistry*. **11**, 1211–1217 (1972).

42. F. Ruhnow, D. Zwicker, S. Diez, Tracking Single Particles and Elongated Filaments with Nanometer Precision. *Biophys. J.* **100**, 2820–2828 (2011).

43. Chen, J., & Gupta, A. K. Testing and Locating Variance Changepoints with Application to Stock Prices. *J. Am. Stat. Assoc.*, **92**, 739 (1997).

44. B. Kalafut, K. Visscher, An Objective, Model-independent Method for Detection of Non-uniform Steps in Noisy Signals. *Computer Physics Communications*. **179(10),** 716-723 (2008).

45. K. C. Holmes, D. Popp, W. Gebhard, W. Kabsch, Atomic Model of the Actin Filament. *Nature*. **347**, 44–49 (1990).

46. T. D. Pollard, M. S. Mooseker, Direct Measurement of Actin Polymerization Rate Constants by Electron-Microscopy of Actin-Filaments Nucleated by Isolated Microvillus Cores. *J. Cell Biol.* **88**, 654–659 (1981).

47. T. D. Pollard, Rate Constants for the Reactions of ATP-Actin and ADP-Actin with the Ends of Actin-Filaments. *J. Cell Biol.* **103**, 2747–2754 (1986).

48. E. G. Marklund, M. T. Degiacomi, C. V. Robinson, A. J. Baldwin, Benesch, Justin L. P., Collision Cross Sections for Structural Proteomics. *Structure*. **23**, 791–799 (2015).

49. F. Hagn, M. Etzkorn, T. Raschle, G. Wagner, Optimized Phospholipid Bilayer Nanodiscs Facilitate High-Resolution Structure Determination of Membrane Proteins. *J. Am. Chem. Soc.* **135**, 1919–1925 (2013).

50. M. T. Marty *et al.*, Native Mass Spectrometry Characterization of Intact Nanodisc Lipoprotein Complexes. *Anal. Chem.* **84**, 8957–8960 (2012).

51. I. G. Denisov, Y. V. Grinkova, A. A. Lazarides, S. G. Sligar, Directed self-assembly of monodisperse phospholipid bilayer nanodiscs with controlled size. *J. Am. Chem. Soc.* **126**, 3477–3487 (2004).